Handbook of Mathematical Geodesy
Geosystems Mathematics, 687–751

Gravimetry and Exploration

C. Blick, W. Freeden, and H. Nutz

Abstract. In this work we are especially concerned with the "mathematization" of gravimetric exploration and prospecting. We investigate the extractable information of the Earth's gravitational potential and its observables obtained by gravimetry for gravitational modeling as well as geological interpretation. More explicitly, local gravimetric data sets are exploited to visualize multiscale reconstruction and decorrelation features to be found in geophysically and geologically relevant signature bands.

Keywords. Absolute and relative gravimetry, Newtonian gravitational approach, multiscale density field modeling.

Introduction

Newton's famous law about the mutual attraction of two masses formulated in "De mundi systemate" 1715 tells us that the attractive force, called *gravitation*, is directed along the line connecting the two centers of mass of the objects and is proportional to two masses as well as to the squared inverse of the distance between the objects. If the Earth had a perfectly spherical shape and if the mass inside the Earth were distributed homogeneously or rotationally symmetric, the line along which an apple fell would indeed be a straight line, directed radially and going exactly through the Earth's center of mass. The gravitational field obtained in this way would be perfectly spherically symmetric. In reality, however, the situation is more complex. The topographic features, mountains and valleys, are very irregular. The actual gravitational field is influenced by strong irregularities in density within the Earth. As a result, the gravitational force deviates from one place to the other from that of a homogeneous sphere. More explicitly, internal density signatures are reflected in gravitational field signatures, and orthogonal coefficients in terms of spherical harmonics of gravitational field signatures smooth out exponentially with increasing distance from the Earth's body. As a consequence, positioning systems are ideally located as far as possible from the Earth, whereas gravity field sensors are ideally located as close as possible to the Earth. Following these basic

principles, various positioning and gravity field determination techniques have been designed. Sensors may be sensitive to local or global features of the gravity field. Considering the spatial location of the data points, we may differentiate between terrestrial (surface), airborne, and spaceborne methods.

Concerning gravity on a global scale, e.g., for global geoid determination (that will not be investigated here), it should be pointed out (see, e.g., [6–8]) that the terrestrial distribution of Earth's gravity data is far from being homogeneous with large gaps, in particular over oceans but also over land. In addition, the quality of the data is very distinct. Thus, global terrestrial gravity data coverage now and in the foreseeable future is far from being satisfactory. This is the reason why spaceborne measurements come into play for global gravity determination. Until now, the relatively poor precision of satellite-only spaceborne gravity measurements has hindered a wider use of this type of measurements for local purposes. Seen from future exploration aspects, however, it must be remarked that only coordinated research will provide a breakthrough in modeling and understanding significant structures and processes in the Earth's interior. In fact, the authors are convinced that the way forward, even in global modeling, has to be based on two requirements:

i) combining data from different sensors and sources,
ii) multiscale modeling, i.e., "zooming-in downward continuation" of the different data sources starting from globally available spaceborne data as means for an appropriate trend solution via more accurate (regional) airborne data down to (local) high-precision gravimetric data sets.

In this contribution, we are especially concerned with the mathematical study of gravimetry in exploration, in particular postprocessing of all already available models. To this end we briefly explain the status quo of gravimetric observation and standard modeling. On the basis of these results we present new multiscale methods by means of geoscientifically relevant wavelets for the decorrelation of signatures inherent in geological information.

1. Gravity, gravitation, and gravimetry

The force of gravity provides a directional structure to the space above the Earth's surface. It is tangential to the vertical plumb lines and perpendicular to all (level) equipotential surfaces. Any water surface at rest is part of a level surface. (Level) equipotential surfaces are ideal reference surfaces, for example, for heights. The geoid is defined as that level surface of the gravity field which best fits the mean sea level.

The direction of the gravity vector can be obtained by astronomical positioning. Measurements are possible on the Earth's surface. Observations of the gravity vector are converted into so-called vertical deflections by subtracting a corresponding reference direction derived from a simple gravity field model associated to, e.g., an ellipsoidal surface. Vertical deflections are tangential fields

of the anomalous potential. Due to the high measurement effort required to acquire these types of data compared to a gravity measurement, the data density of vertical deflections is much less than that of gravity anomalies. Gravitational field determination based on the observation of deflections of the vertical and combined with gravity is feasible in smaller areas with good data coverage.

1.1. Gravitational, centrifugal, and gravity acceleration

The *gravity acceleration* (*gravity*) w is the resultant of the *gravitation* v and the *centrifugal acceleration* c such that

$$w = v + c. \tag{1.1}$$

The centrifugal force c arises as a result of the rotation of the Earth about its axis. In this work concerned with local gravity exploration we are allowed to assume a rotation of constant angular velocity ω. The centrifugal acceleration acting on a unit mass is directed outward perpendicularly to the spin axis (see Figure 1.1). Introducing the so-called *centrifugal potential* C, such that $c = \nabla C$, the function C turns out to be non-harmonic. The direction of the gravity w is known as the direction of the *plumb line*, the quantity $|w|$ is called the *gravity intensity* (often also just called *gravity* and denoted in the geodetic jargon by g). Altogether, the *gravity potential of the Earth* can be expressed in the form

$$W = V + C, \tag{1.2}$$

and the gravity acceleration w is given by

$$w = \nabla W = \nabla V + \nabla C. \tag{1.3}$$

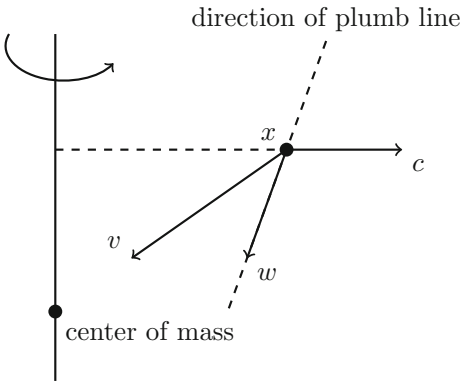

FIGURE 1.1. Gravitation v, centrifugal acceleration c, gravity acceleration w.

As already pointed out, the surfaces of constant gravity potentials, i.e., $W =$ const., are designated as *equipotential* (*level,* or *geopotential*) *surfaces of gravity* (for more details, the reader is referred to monographs in physical geodesy, e.g., [27, 32, 51, 69]).

The actual Earth's surface (globally available from modern spaceborne techniques such as DOPPLER, GNSS, LASER, VLBI, etc.) does not coincide with an equipotential surface (i.e., a level surface). The force of gravity is generally not perpendicular to the actual Earth's surface (see Figure 1.2). However, we are confronted with the gravity intensity as an oblique derivative on the Earth's surface. The gravity vector is an oblique vector at any point on the Earth's surface and generally not the normal vector.

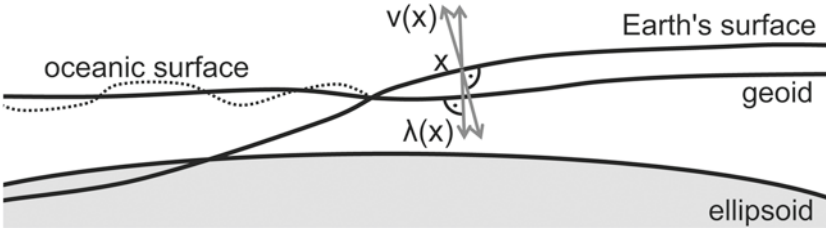

FIGURE 1.2. Earth's surface, geoid, ellipsoid ($\lambda = \frac{w}{|w|}$ oblique unit gravity vector, normal vector to the geoid, but usually not normal to the Earth's surface).

The determination of equipotential surfaces of the potential W is strongly related to the knowledge of the potential V. The gravity vector w given by $w = \nabla W$ is normal to the equipotential surface passing through the same point. Thus, equipotential surfaces such as the geoid intuitively express the notion of tangential surfaces, as they are normal to the plumb lines given by the direction of the gravity vector.

1.2. Gravimeter and gravimetry

Essentially, the Earth is a "spheroid", with a slight flattening (0.35%) at the poles, a mean radius of 6368km, and a mean mass of $5.98 \cdot 10^{24}$kg. At the surface of the Earth, its mean value of gravity intensity is given by $9.80\frac{m}{s^2}$. At the equator, it reduces to $9.78\frac{m}{s^2}$; at the poles, it increases to about $9.83\frac{m}{s^2}$, reflecting the flattening.

Gravimeters are typically designed to measure very tiny fractional changes of the Earth's gravity, caused by nearby geologic structures or the shape of the Earth. There are two types of gravimeters, viz. *relative* and *absolute gravimeters*. Absolute gravimeters measure the local gravity and are directly based on measuring the acceleration of free fall (for example, of a test mass in a vacuum tube). Relative gravimeters compare the value of gravity at one point with another. They must be calibrated at a location, where the gravity is known accurately and measure the ratio of the gravity at the two points. Most common relative gravimeters are spring-based. By determining the amount by which the weight stretches the spring, gravity becomes available via Hooke's law (see Figure 1.3). The highest possible accuracy of relative gravity measurements are conducted at the Earth's surface. Measurements on ships and in aircrafts deliver reasonably good data only after the removal of inertial noise. In addition, when interested in gravimetric exploration,

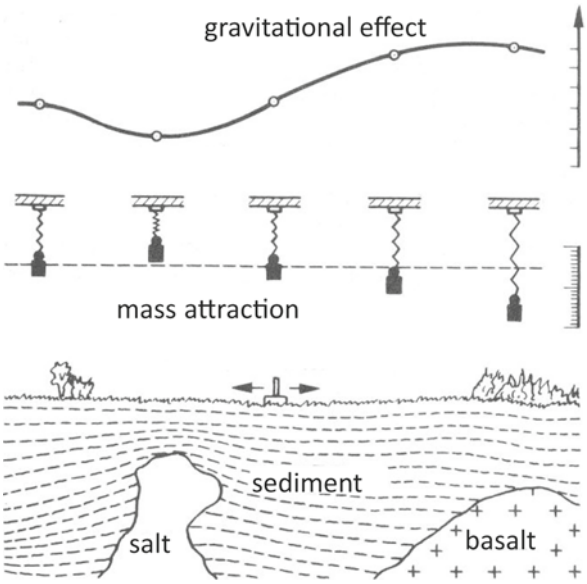

FIGURE 1.3. The principle of gravimetry (with kind permission of Teubner-publishing taken from [38] in modified form).

it should be noted that a high measurement accuracy of at least 0.1mGals, but more adequately 0.01mGals ($1\,\text{mGal} = 10^{-5}\frac{m}{s^2}$, cf. Table 1) has to be achieved (cf. Figure 1.4).

SI Units	Traditional Units
$10^{-2}ms^{-2}$	1 Gal
$10^{-5}ms^{-2}$	1 mGal
$10^{-8}ms^{-2}$	1 μGal

TABLE 1. Traditional units for gravimetric measurements and their SI unit complement.

By *gravimetry*, we denote the determination of the Earth's mass density distribution from data of the gravitational potential or related quantities. Clearly, for purposes of exploration, it is obvious that the determination of gravity intensities as well as gravity anomalies of dimension very much larger than the gravity anomalies caused by, e.g., aquifers, oil and gas structures are of less significance. The fundamental interest in gravimetric methods in exploration is based on the measurements of small variations.

Gravity prospecting has been first used in the case of strong density contrasts in a geological structure, and the usual approach is to measure differences in gravity from place to place. Today, the interpretation of gravimetric data is done by comparing the shape and size of gravity disturbances and anomalies to those

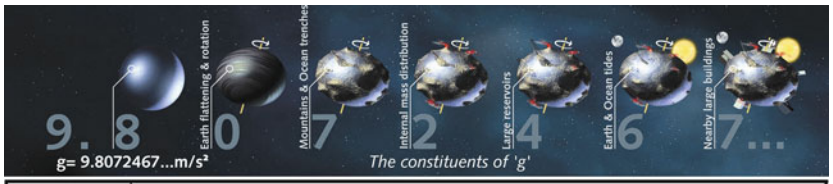

10^{0}	Spherical Earth
10^{-3}	Flattening & Centrifugal Acceleration
10^{-4}	Mountains, Valleys, Oceanic Ridges, Subduction
10^{-5}	Density Variations in Crust and Mantle
10^{-6}	Salt Domes, Sedimentary Basins, Deposits
10^{-7}	Tide, Atmospherical Pressure
10^{-8}	Temporal Variations: Oceans, Hydrology
10^{-9}	Ocean Topography, Movement of Poles

FIGURE 1.4. Illustration of the components of the gravity acceleration (ESA medialab, ESA communication production SP–1314).

caused by bodies of various geometrical shapes at different depths and differing densities.

The observed gravity depends on the following effects to be removed (for more detailed studies, see, e.g., [53, 59, 64]): attraction of the reference ellipsoid, elevation above sea level, topography, time dependent variations (tidal), (Eőtvős) effect of a moving platform, isostatic balance on the lower lithosphere, density variations inside the upper crust. To isolate the effects of local density variations from all other contributions, it is necessary to apply a series of reductions: The attraction of, e.g., the reference ellipsoid or another reference surface has to be subtracted from the measured values. An elevation correction must be done, i.e., the vertical gradient of gravity is multiplied by the elevation of the station and the result is added. With increasing elevation of the Earth, there is usually an additional mass between the reference level and the actual level. This additional mass itself exerts a positive gravitational attraction. Bouguer correction and terrain correction are applied to correct for the attraction of the slab of material between the observation point and the geoid. A terrain correction accounts for the effect of nearby masses above or mass deficiencies below the station. Isostatic correction accounts for the isostatic roots (Moho). Other corrections have to be applied to the data in order to account for effects not related to the subsurface: Drift corrections are necessary, since each gravimeter suffers mechanical changes over time, and so does its output measurement. This change is generally assumed

to be linear. Tidal corrections have to be imposed, i.e., the attraction of the Sun and Moon has to be calculated and subtracted from the measurements. In case of acquisition on a moving platform, the motion relative to the surface of the Earth implies a change in centrifugal acceleration. The Eőtvős correction depends on the latitude and velocity vector of the moving platform. It should be observed that free air anomaly does not correct for the first two effects which could mask the gravity anomalies related to the Bouguer density contrasts in the crust. Complete Bouguer correction effectively remove the gravity anomalies due to bathymetry, but still contain the gravity effect of the Moho. Isostatics contain the gravity effect of the Moho. For more details the reader is referred to geodetic textbooks such as [32, 36, 68] and to the literature concerned with prospecting and exploration (see, e.g., [53, 54, 64] and the references therein).

Gravity prospecting can be done over land or sea areas using different techniques and equipment. Terrestrial gravimetry was first applied *to prospect for salt domes* (*e.g., in the Gulf of Mexico*) (an example of the Eastern part of Germany is shown in Figure 1.5), and later for looking for *anticlines in continental areas* (see, e.g., [53, 54], and the references therein). Nowadays, gravimetry is in use all over the world in diverse applications:

(1) Gravimetric surveys serve regional geological mapping.
(2) Gravimetry is helpful in different phases of the oil exploration and production processes.
(3) Gravimetric surveys are employed in mineral exploration, for example, to detect mineral deposits (see Figure 1.5) of economic interest (such as metals, salt, coal).
(4) Archaeological and geotechnical studies aim at the mapping of subsurface voids and overburden variations.
(5) Gravimetric campaigns may be applied for groundwater and environmental studies. They help to map aquifers to provide formations and/or structural control.
(6) Gravimetric studies give information about tectonically derived changes and volcanological phenomena.
(7) Gravimetric studies provide useful information on changes in the level of water in geothermal reservoirs and therefore on the longevity of a geothermal resource.

It is surprising that the use of gravimetry is in infancy in the German geothermal scene, although it has much to offer. Due to (regional) airborne and (global) spaceborne gravity information such as satellite-to-satellite tracking (SST) and/or satellite gravity gradiometry (SGG), new promising components in gravimetrically oriented modeling can be expected in the future, for example, based on multiscale modeling providing reconstruction and decomposition of geological signatures, where seismic modeling is difficult or impossible because of anthropogenic activities, e.g., in mining areas.

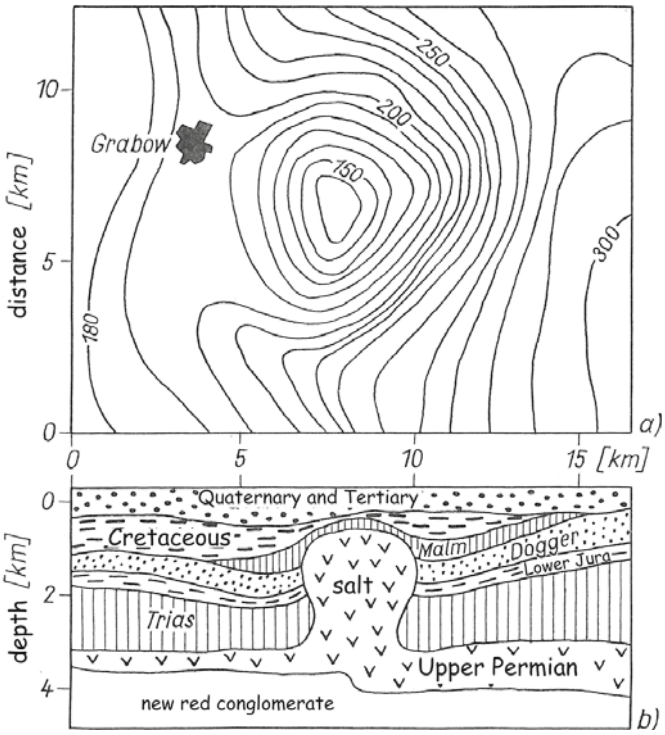

FIGURE 1.5. Top: Gravity effect in $[\mu m \cdot s^{-1}]$ of the salt dome Werle (Mecklenburg, Germany); bottom: Geological vertical profile (with kind permission of Teubner-publishing taken from [38] in modified form).

All in all, nowadays the main applications of gravimetry can be listed as follows:

(i) definition of geological structural settings,
(ii) faults delineation,
(iii) recovery of salt bodies, metal deposits,
(iii) detection of heap of coal, ore, etc.,
(iv) 2D/3D forward modeling, inversion, and postprocessing to assist seismic modeling,
(v) combination with geomagnetic interpretation,
(vi) 4D monitoring, etc.

Figure 1.6 shows the gravity as well as the vertical/horizontal gradient curves induced by a simple geological structure in sectional illustration (for similar illustrations, the reader is referred to, e.g., [5, 26, 39, 48, 53, 54, 64]). It is remarkable that the vertical/horizontal gradient curves show significant interactions on density variations.

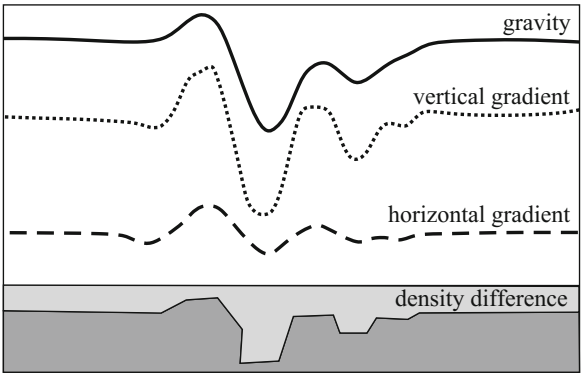

FIGURE 1.6. Schematic diagram of the horizontal/vertical gradients vs. the gravity potential (cf. [54]).

The knowledge of horizontal/vertical derivatives of the gravity potential is therefore a useful addendum to prospecting and exploration. This is the reason why we are interested in discussing these derivatives in more detail (based on ideas and concepts developed in [15]).

2. Surface horizontal/vertical derivatives of the gravity potential

The lines that intersect all equipotential surfaces orthogonally are not exactly straight but slightly curved (cf. Figure 2.1). They are called lines of gravity force or *plumb lines*. The gravity vector at any point is tangential to the plumb line. Hence, "direction of the gravity vector", "vertical" and "direction of the plumb line" are synonymous. As the equipotential surfaces are, so to speak, "horizontal", i.e., orthogonal to the plumb lines, they play an important part in our daily life (e.g., in civil engineering for the purpose of height determination). Equipotential surfaces of the Earth's gravity potential W allow, in general, no simple mathematical representation. This is the reason why physical geodesy and geophysics choose a suitable reference surface for modeling the geoid, i.e., the equipotential surface at sea level. The reference surface is constructed as an equipotential surface of an artificial *normal gravity potential* U . Its gradient field, i.e., $u = \nabla U$, is called *normal gravity*. For reasons of simplicity, physical geodesy usually uses an ellipsoid of revolution in such a way that a good adaption to the Earth's surface is guaranteed. Closed representations of normal gravity potentials, in consideration of the centrifugal force, can be found extensively in the geodetic literature (cf. [25, 27, 32, 36, 45, 51, 65]), and the references therein). The deviations of the gravity field of the Earth from the normal field of such an ellipsoid are small. The remaining parts of the gravity field are gathered in a so-called *disturbing gravity field* ∇T corresponding to the *disturbing potential* $T = W - U$.

2.1. Gravity anomalies, gravity disturbances, and vertical deflections

Knowing the gravity potential, all equipotential surfaces (including the geoid) are given by an equation of the form $W(x) = \text{const}$. By introducing U as the normal gravity potential corresponding to the ellipsoidal field, the disturbing potential T is the difference of the gravity potential W and the normal gravity potential U, i.e., we are led to a decomposition of the gravity potential in the form $W = U + T$. According to the concept developed by Stokes [65], Helmert [33], and Pizzetti [56, 57] we may assume that

(a) the center of the ellipsoid coincides with the center of gravity of the Earth,
(b) the difference of the mass of the Earth and the mass of the reference body (ellipsoid) is zero.

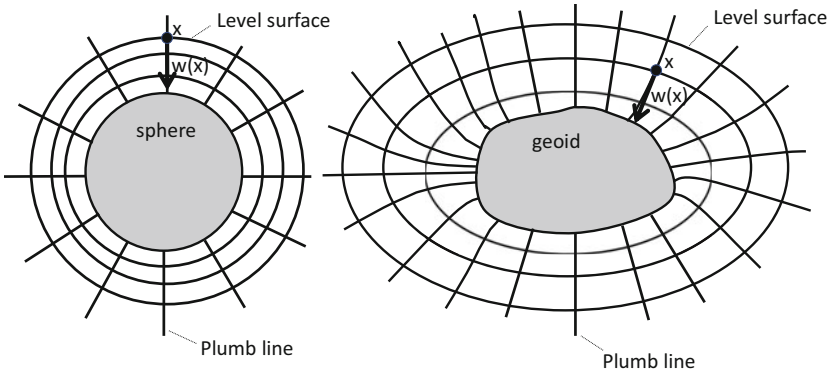

FIGURE 2.1. Level surfaces and plumb lines for a homogeneous ball (left) and an Earth-like body (right) (from [15]).

A point x of the geoid can be projected onto its associated point y of the ellipsoid by means of the ellipsoidal normal. The distance $N(x)$ between x and y is called the *geoidal height* or *geoidal undulation* in x (cf. Figure 2.2). The *gravity anomaly vector* $a(x)$ at the point x of the geoid is defined as the difference between the gravity vector $w(x)$ and the normal gravity vector $u(y)$, i.e.,

$$a(x) = w(x) - u(y). \tag{2.1}$$

Another possibility is to form the difference between the vectors w and u at the same point x such that we get the *gravity disturbance vector* $d(x)$ defined by

$$d(x) = w(x) - u(x). \tag{2.2}$$

In geodesy, several basic mathematical relations between the scalar fields $|w|$ and $|u|$ as well as between the vector fields a and d are known. In the following, we only describe the fundamental relations heuristically (see also [27, 32]).

The point of departure for our excursion into geodesy is the observation that the gravity disturbance vector $d(x)$ at the point x on the geoid can be written as

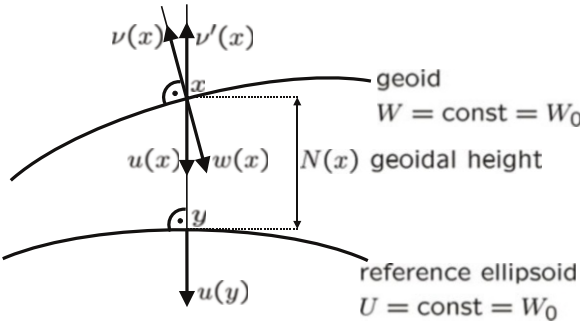

FIGURE 2.2. Illustration of the gravity vector $w(x)$, the normal gravity vector $u(x)$, and the geoidal height $N(x)$. Here, ν and ν' denote the normal to the geoid and the reference ellipsoid, respectively (following [32]).

follows:

$$d(x) = w(x) - u(x) = \nabla\left(W(x) - U(x)\right) = \nabla T(x). \tag{2.3}$$

According to Taylor's formula, $U(y)+\frac{\partial U}{\partial \nu'}(y)N(x)$ is the linearization of $U(x)$, i.e., by expanding the potential U at the point x and truncating the Taylor series at the linear term, we get

$$U(x) \simeq U(y) + \frac{\partial U}{\partial \nu'}(y)N(x), \tag{2.4}$$

where

$$\nu'(y) = -\frac{u(y)}{|u(y)|} \tag{2.5}$$

is the ellipsoidal normal at y and the geoidal undulation $N(x)$ is the aforementioned distance between x and y (note that the symbol '$\simeq$' means that the error between the left- and the right-hand side may be assumed to be insignificantly small). Using the fact that $T(x) = W(x) - U(x)$ and observing the relations

$$|u(y)| = -\nu'(y)\cdot u(y) = -\nu'(y)\cdot \nabla U(y) = -\frac{\partial U}{\partial \nu'}(y), \tag{2.6}$$

we obtain under the assumption of (2.4) that

$$N(x) = \frac{U(y) - U(x)}{|u(y)|} = \frac{T(x) - (W(x) - U(y))}{|u(y)|}. \tag{2.7}$$

Finally, considering $U(y) = W(x) = \text{const.} = W_0$, we end up with the so-called *Bruns formula* (cf. [4])

$$N(x) = \frac{T(x)}{|u(y)|}. \tag{2.8}$$

This formula relates the physical quantity $T(x)$ to the geometric quantity $N(x)$ for points x on the geoid.

It is helpful to study the vector field $\nu(x)$ in more detail:

$$\nu(x) = -\frac{w(x)}{|w(x)|}. \tag{2.9}$$

Due to the definition of the normal vector field (2.9), we obtain the following identity

$$w(x) = \nabla W(x) = \ - \ |w(x)| \ \nu(x). \tag{2.10}$$

In an analogous way we obtain

$$u(x) = \nabla U(x) = \ - \ |u(x)| \ \nu'(x). \tag{2.11}$$

The *vertical deflection* $\Theta(x)$ at the point x on the geoid is understood to be the angular (i.e., tangential) difference between the directions $\nu(x)$ and $\nu'(x)$. More concretely, the vertical deflection is determined by the angle between the plumb line and the ellipsoidal normal through the same point:

$$\Theta(x) = \nu(x) - \nu'(x) - ((\nu(x) - \nu'(x)) \cdot \nu(x))\, \nu(x). \tag{2.12}$$

According to its construction, the vertical deflection $\Theta(x)$ at x is orthogonal to the normal vector field $\nu(x)$, i.e., $\Theta(x) \cdot \nu(x) = 0$. Since the plumb lines are orthogonal to the equipotential surfaces of the geoid and the ellipsoid, respectively, the vertical deflection gives briefly spoken a measure of the gradient of the equipotential surfaces (cf. [32]). From (2.10), in connection with (2.12), it follows that

$$w(x) = -|w(x)|\, (\Theta(x) + \nu'(x) + ((\nu(x) - \nu'(x)) \cdot \nu(x))\, \nu(x))\,. \tag{2.13}$$

Using Eqs. (2.11) and (2.13) we finally obtain for the gravity disturbing vector $d(x)$ at the point x

$$\begin{aligned} d(x) = \nabla T(x) &= w(x) - u(x) \qquad (2.14)\\ &= -|w(x)|\, (\Theta(x) + \nu'(x) + ((\nu(x) - \nu'(x)) \cdot \nu(x))\, \nu(x)) - (-|u(x)|\nu'(x))\\ &= -|w(x)|\, (\Theta(x) + ((\nu(x) - \nu'(x)) \cdot \nu(x))\, \nu(x)) - (|w(x)| - |u(x)|)\, \nu'(x). \end{aligned}$$

The quantity

$$D(x) = |w(x)| - |u(x)| \tag{2.15}$$

is called the *gravity disturbance*, whereas

$$A(x) = |w(x)| - |u(y)| \tag{2.16}$$

is called the *gravity anomaly*.

Splitting the gradient $\nabla T(x)$ of the disturbing potential T at x into a normal part (pointing into the direction of $\nu(x)$) and an angular (tangential) part (using the representation of the surface gradient ∇^*), we have

$$\nabla T(x) = \nu(x) \frac{\partial T}{\partial \nu}(x) + \frac{1}{|x|} \nabla^* T(x), \tag{2.17}$$

where ∇^* is the surface gradient.

Since the gravity disturbances represent at most a factor 10^{-4} of the Earth's gravitational force (for more details see [32]), the error between $\nu(x)\frac{\partial T}{\partial \nu}(x)$ and $\nu'(x)\frac{\partial T}{\partial \nu'}(x)$ has no (computational) significance. Consequently, we may assume

$$d(x) \simeq \nu'(x)\frac{\partial T}{\partial \nu'}(x) + \frac{1}{|x|}\nabla^* T(x). \tag{2.18}$$

Moreover, the scalar product $(\nu(x) - \nu'(x)) \cdot \nu(x)$ can also be neglected. Thus, in connection with (2.14), we obtain

$$d(x) \simeq -|w(x)|\ \Theta(x) - D(x)\nu'(x). \tag{2.19}$$

By comparison of (2.18) and (2.19), we therefore get

$$D(x) = -\frac{\partial T}{\partial \nu'}(x) = -\nu'(x) \cdot d(x), \tag{2.20}$$

$$|w(x)|\ \Theta(x) = -\frac{1}{|x|}\nabla^* T(x). \tag{2.21}$$

In other words, the gravity disturbance $D(x)$, beside being the difference in magnitude of the actual and the normal gravity vector, is also the normal component of the gravity disturbance vector $d(x)$. In addition, we are led to the angular differential equation (2.21).

Applying Bruns' formula (2.8) to Eqs. (2.20) and (2.21) we obtain

$$D(x) = |w(x)| - |u(x)| = -|u(y)|\ \frac{\partial N}{\partial \nu'}(x) \tag{2.22}$$

for the gravity disturbance and

$$|w(x)|\ \Theta(x) = -\frac{1}{|x|}\ \nabla^* T(x) = -\frac{1}{|x|}|u(y)|\ \nabla^* N(x) \tag{2.23}$$

for the vertical deflections. Note that $\Theta(x)$ may be multiplied (without loss of (computational) precision) either by $|w(x)|$ or by $|u(x)|$ since it is a small quantity.

Turning over to the gravity anomalies $A(x)$, it follows from the identity (2.20) by linearization that

$$-\frac{\partial T}{\partial \nu'}(x) = D(x) \simeq A(x) - \frac{\partial |u(y)|}{\partial \nu'}N(x). \tag{2.24}$$

Using Bruns' formula (2.8), we obtain for the gravity anomalies that

$$A(x) = -\frac{\partial T}{\partial \nu'}(x) + \frac{1}{|u(y)|}\frac{\partial |u(y)|}{\partial \nu'}T(x). \tag{2.25}$$

Summing up our results (2.20) for the gravity disturbance $D(x)$ and (2.25) for the gravity anomaly $A(x)$, we are led to the so-called *fundamental equations of*

physical geodesy:

$$D(x) = |w(x)| - |u(x)| = -\frac{\partial T}{\partial \nu'}(x), \tag{2.26}$$

$$A(x) = |w(x)| - |u(y)| = -\frac{\partial T}{\partial \nu'}(x) + \frac{1}{|u(y)|}\ \frac{\partial |u(y)|}{\partial \nu'}\ T(x). \tag{2.27}$$

Eqs. (2.26) and (2.27) show the relation between the disturbing potential T and the gravity disturbance D and the gravity anomaly A, respectively, on the geoid (see, for example, [27, 32, 45]). They are used as boundary conditions in boundary-value problems.

Remark 2.1. Following [32], the geoidal heights N, i.e., the deviations of the equipotential surface on the mean ocean level from the reference ellipsoid, are extremely small. Their order is of only a factor 10^{-5} of the Earth's radius (see [32] for more details). Even more, the reference ellipsoid only differs from a sphere Ω_R with (mean Earth's) radius R in the order of the flattening of about $3 \cdot 10^{-3}$. Therefore, since the time of [65], it is common use that, in theory, an ellipsoidal reference surface should be taken into account. However, in numerical practice, the reference ellipsoid is treated as a sphere and the Equations (2.22) and (2.23) are solved in spherical approximation. In doing so, a relative error of the order of the flattening of the Earth's body at the poles, i.e., a relative error of 10^{-3}, is accepted in all equations containing the disturbing potential. Considering appropriately performed reductions in numerical calculations, this error seems to be quite permissible (cf. [32] and the remarks in [24, 25] for comparison with ellipsoidal approaches), and this is certainly the case if local exploration is under consideration. For local purposes as discussed in this contribution, the problem of non-ellipticity seems to be obsolete.

Remark 2.2. According to the Pizzetti assumptions (see [56, 57]), it follows that the first moment integrals of the disturbing potential vanish, i.e.,

$$\int_{\Omega_R} T(y) H^R_{-n-1,k}(y)\, d\omega(y) = 0, \tag{2.28}$$

for $n = 0, 1,\ k = 1, \ldots, 2n+1$, where $H^R_{-n-1,k}$ denotes the system of outer harmonics and $d\omega$ is the surface element in $\mathbb{R}^3$. More concretely, if the Earth's center of gravity is the origin, there are no first-degree terms in the spherical harmonic expansion of T. If the mass of the spherical Earth and the mass of the normal ellipsoid is equal, there is no zero term. In this way, together with the indicated processes in gravitational modeling, formulas and structures are obtained that are rigorously valid for the sphere.

In the well-known spherical nomenclature, involving a sphere Ω_R as reference surface (R being the mean Earth's radius) with a mass M distributed homoge-

neously in its interior, we are simply led to (cf. [32])

$$U(y) = \frac{\gamma M}{|y|}, \qquad u(y) = \nabla U(y) = -\frac{\gamma M}{|y|^2}\frac{y}{|y|}, \tag{2.29}$$

where γ is the gravitational constant ($\gamma = 6.6742 \cdot 10^{-11}\mathrm{m}^3\ \mathrm{kg}^{-1}\ \mathrm{s}^{-2}$). Hence, we obtain

$$|u(y)| = \frac{\gamma M}{|y|^2}, \tag{2.30}$$

$$\frac{\partial |u(y)|}{\partial \nu'} = -\frac{u(y)}{|u(y)|} \cdot \nabla |u(y)| = -2\frac{\gamma M}{|y|^3}, \tag{2.31}$$

$$\frac{1}{|u(y)|}\frac{\partial |u(y)|}{\partial \nu'} = -\frac{2}{|y|}, \tag{2.32}$$

where x is on the geoid and y is on the reference surface (cf. Fig. 2.2). Furthermore, in spherical nomenclature, i.e., $x \in \Omega_R$, we obviously have

$$-\frac{\partial T}{\partial \nu'}(x) = -\frac{x}{|x|} \cdot \nabla T(x). \tag{2.33}$$

Therefore, we end up with the formulation of the *fundamental equations of physical geodesy for the sphere*:

$$D(x) = -\frac{x}{|x|} \cdot \nabla T(x), \tag{2.34}$$

$$A(x) = -\frac{x}{|x|} \cdot \nabla T(x) - \frac{2}{|x|} T(x). \tag{2.35}$$

In addition, in a vector spherical context (see also [22]), we obtain for the differential equation (2.21)

$$-\nabla^* T(x) = \frac{\gamma M}{R} \Theta(x), \tag{2.36}$$

and, by virtue of Bruns' formula (2.8), we finally find that

$$-\nabla^* N(x) = R\Theta(x). \tag{2.37}$$

Remark 2.3. In physical geodesy (see, e.g., [32, 36]), a componentwise scalar determination of the vertical deflection is usually used. Our work prefers the vectorial framework, i.e., the vector equation (2.36). In doing so, we are concerned with an isotropic vector approach by means of the fundamental solution with respect to the Beltrami operator (see also [22]) instead of the conventional anisotropic scalar decomposition into vector components due to [44].

The disturbing potential enables us to make the following *geophysical interpretations* (for more details the reader is referred, e.g., [25, 41, 60, 63], and the references therein): Gravity disturbances D and gravity anomalies A (Figure 2.3) represent a relation between the real Earth and an ellipsoidal Earth model. In accordance with Newton's Law of Gravitation they therefore show the imbalance of forces in the interior of the Earth due to the irregular density distribution

inside the Earth. Clearly, gravity anomalies and/or gravity disturbances do not determine uniquely the interior density distribution of the Earth. They may be interpreted as certain filtered signatures, which give major weight to the density contrasts close to the surface and simultaneously suppress the influence of deeper structures inside the Earth.

Geoid undulations provide a measure for the perturbations of the Earth from a hydrostatic equilibrium. They form the deviations of the equipotential surfaces at mean sea level from the reference ellipsoid. Geoid undulations show no essential correlation to the distributions of the continents. They seem to be generated by density contrasts much deeper inside the Earth.

As already explained, the task of determining the disturbing potential T from gravity disturbances or gravity anomalies, respectively, leads to boundary-value problems usually corresponding to a spherical boundary. Numerical realizations of such boundary-value problems have a long tradition, starting from [65] and [55]. Nonetheless, our work presents some new aspects in their potential theoretic treatment by proposing appropriate space-regularization techniques applied to the resulting integral representations of their solutions. For both boundary-value problems, viz. the Neumann and the Stokes problem, we are able to present two solution methods: The disturbing potential may be either solved by a Fourier (orthogonal) expansion method in terms of spherical harmonics or it can be described by a singular integral representation over the boundary Ω_R.

Remark 2.4. So far, much more data on gravity anomalies $A(x) = |w(x)| - |u(y)|$ are available than on gravity disturbances $D(x) = |w(x)| - |u(x)|$. However, by modern GNSS-technology (see, e.g., [52]), the point x on the geoid is rather determined than y on the reference ellipsoid. Therefore, in future, it can be expected that D will become more important than A (as [36] point out in their monograph on physical geodesy). This is the reason why we continue to work with D. Nevertheless, the results of our (multiscale) approach applied to A are of significance. Therefore, the key ideas and concepts concerning A can be treated in parallel (see [9, 15, 73] for explicit details).

In order to formulate some results in the language of potential theory, we first introduce the potential space $\mathrm{Pot}^{(1)}\left(\mathbb{R}^3\backslash\mathcal{B}_R(0)\right)$, where $\mathcal{B}_R(0)$ is the (open) ball of radius R around the origin. More concretely, we let $\mathrm{Pot}(\mathbb{R}^3\backslash\overline{\mathcal{B}_R(0)})$ be the space of all functions $F : \mathbb{R}^3\backslash\overline{\mathcal{B}_R(0)} \to \mathbb{R}$ satisfying

(i) $F|_{\mathbb{R}^3\backslash\overline{\mathcal{B}_R(0)}}$ is a member of $C^{(2)}(\mathbb{R}^3\backslash\overline{\mathcal{B}_R(0)})$,
(ii) F satisfies Laplace's equation $\Delta F(x) = 0$, $x \in \mathbb{R}^3\backslash\overline{\mathcal{B}_R(0)}$.
(iii) F is regular at infinity, i.e., $F(x) = O(|x|^{-1})$, $|x| \to \infty$.

$\mathrm{Pot}^{(1)}(\mathbb{R}^3\backslash\mathcal{B}_R(0))$ is formally understood to be the space

$$\mathrm{Pot}^{(1)}\left(\mathbb{R}^3\backslash\mathcal{B}_R(0)\right) = C^{(1)}\left(\mathbb{R}^3\backslash\mathcal{B}_R(0)\right) \cap \mathrm{Pot}(\mathbb{R}^3\backslash\overline{\mathcal{B}_R(0)}). \tag{2.38}$$

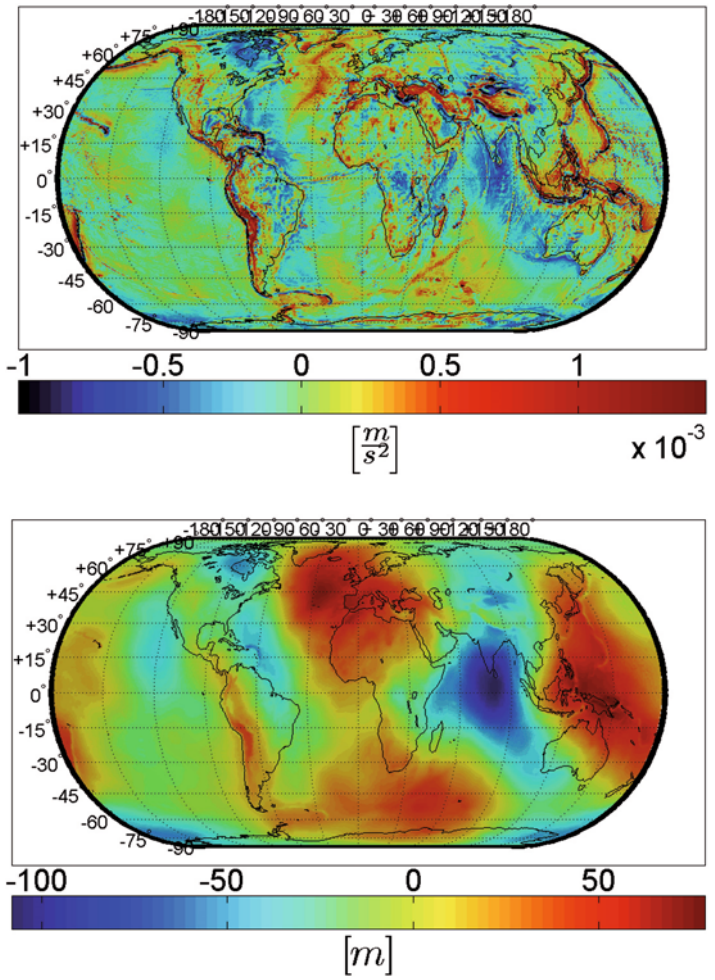

FIGURE 2.3. EIGEN-GL04C derived gravity anomalies and geoidal undulations (reconstructed by use of (spherical) smoothed Haar scaling functions from [22] based on computations by Mathar [43]).

In the language of potential theory, the *exterior Neumann boundary-value problem* corresponding to known gravity disturbances D (compare (2.34)) reads as follows:

(ENPPG) Let D be a continuous function on $\Omega_R = \partial\mathcal{B}_R(0)$, i.e., $D \in C^{(0)}(\Omega_R)$ with

$$\int_{\Omega_R} D(y) H^R_{-n-1,k}(y)\, d\omega(y) = 0, \tag{2.39}$$

for $n = 0, 1,\ k = 1, \dots, 2n+1$. Find $T \in \mathrm{Pot}^{(1)}\left(\mathbb{R}^3 \backslash \mathcal{B}_R(0)\right)$, such that the boundary condition $D = \frac{\partial T}{\partial \nu}\big|_{\Omega_R}$ holds true and the potential T fulfills the conditions

$$\int_{\Omega_R} T(y) H^R_{-n-1,k}(y)\, d\omega(y) = 0 \tag{2.40}$$

for $n = 0, 1,\ k = 1, \dots, 2n+1$.

It is known (see, e.g., [15]) that the solution of the boundary-value problem (ENPPG) can be represented in the form

$$T(x) = \frac{1}{4\pi R} \int_{\Omega_R} D(y)\ N(x,y)\ d\omega(y), \qquad x \in \mathbb{R}^3 \backslash \mathcal{B}_R(0), \tag{2.41}$$

where the *Neumann kernel* $N(\cdot,\cdot)$ in (2.41) possesses the spherical harmonic expansion

$$N(x,y) = \sum_{n=2}^{\infty} \left(\frac{R^2}{|x||y|}\right)^{n+1} \frac{2n+1}{n+1} P_n\left(\frac{x}{|x|} \cdot \frac{y}{|y|}\right). \tag{2.42}$$

By well-known manipulations, the series in terms of Legendre polynomials can be expressed as an elementary function leading to the integral representation

$$T(x) = \frac{1}{4\pi R} \int_{\Omega_R} D(y) \left(\frac{2R}{|x-y|} + \ln\left(\frac{|y| + \left|y - \frac{R^2}{|x|^2}x\right| - \frac{R^2}{|x|}}{|y| + \left|y - \frac{R^2}{|x|^2}x\right| + \frac{R^2}{|x|}}\right)\right) d\omega(y). \tag{2.43}$$

It is not difficult to see that for $x \in \Omega_R$, the integral (2.43) is equivalent to

$$T(x) = \frac{1}{4\pi R} \int_{\Omega_R} D(y) \left(\frac{2R}{|x-y|} + \ln\left(\frac{|y| + |x-y| - R}{|y| + |x-y| + R}\right)\right) d\omega(y). \tag{2.44}$$

Written out in spherical nomenclature $x = R\frac{x}{|x|}$, $y = R\frac{y}{|y|}$, $x \neq y$ on Ω_R, we find

$$N\left(R\frac{x}{|x|}, R\frac{y}{|y|}\right) = \frac{2}{\left|\frac{x}{|x|} - \frac{y}{|y|}\right|} + \ln\left(\frac{R\left|\frac{x}{|x|} - \frac{y}{|y|}\right|}{2R + R\left|\frac{x}{|x|} - \frac{y}{|y|}\right|}\right). \tag{2.45}$$

If we use

$$\left|\frac{x}{|x|} - \frac{y}{|y|}\right| = \left(2 - 2\frac{x \cdot y}{|x|\ |y|}\right)^{\frac{1}{2}}, \tag{2.46}$$

then, for $x \neq y$, we are led to the identity

$$\begin{aligned} N\left(R\frac{x}{|x|}, R\frac{y}{|y|}\right) &= N\left(\frac{x}{|x|}, \frac{y}{|y|}\right) \\ &= \frac{\sqrt{2}}{\sqrt{1 - \frac{x}{|x|} \cdot \frac{y}{|y|}}} - \ln\left(1 + \frac{\sqrt{2}}{\sqrt{1 - \frac{x}{|x|} \cdot \frac{y}{|y|}}}\right). \end{aligned} \tag{2.47}$$

Consequently, for points $x \in \Omega_R$, we (formally) get the so-called *Neumann formula*, which constitutes an improper integral over Ω_R:

$$T\left(R\frac{x}{|x|}\right) = \frac{1}{4\pi R}\int_{\Omega_R} D\left(R\frac{y}{|y|}\right) N\left(\frac{x}{|x|}, \frac{y}{|y|}\right)\, d\omega(y), \tag{2.48}$$

where the Neumann kernel constitutes a radial basis function due to (2.47).

Once more, in accordance with the conventional approach of physical geodesy, the Neumann formula (2.48) is valid under the following constraints (see also [23, 32, 51]):

(i) the mass within the reference ellipsoid is equal to the mass of the Earth,
(ii) the center of the reference ellipsoid coincides with the center of the Earth,
(iii) the formulation is given in the spherical context to guarantee economical and efficient numerics.

Note that we are able to set $N(R\xi, R\eta) = N(\xi, \eta) = N(\xi \cdot \eta)$ in terms of the unit vectors $\xi = \frac{x}{|x|}$ and $\eta = \frac{y}{|y|}$ which simplifies our notation: If we define the single-layer kernel $S : [-1, 1) \to \mathbb{R}$ by

$$S(t) = \frac{\sqrt{2}}{\sqrt{1-t}}, \qquad t \in [-1, 1), \tag{2.49}$$

the Neumann kernel is the zonal function of the form

$$N(\xi \cdot \eta) = S(\xi \cdot \eta) - \ln\left(1 + S(\xi \cdot \eta)\right), \qquad 1 - \xi \cdot \eta > 0. \tag{2.50}$$

An equivalent formulation of the improper integral (2.48) over the unit sphere $\Omega = \partial\mathcal{B}_1(0)$ is then given by

$$T(R\xi) = \frac{R}{4\pi}\int_{\Omega} D(R\eta) N(\xi \cdot \eta)\, d\omega(\eta). \tag{2.51}$$

It should be remarked that the exterior Stokes boundary value problem of determining the disturbing potential from known gravity anomalies can be handled in a quite analogous way (see [9, 15, 73]), providing the so-called Stokes integral associated to the radially symmetric Stokes kernel as an improper integral on Ω_R.

Next we deal with the vertical deflections Θ (cf. [15, 21]). Suppose that T fulfills the conditions (2.40). We consider the differential equation (compare Eq. (2.36))

$$\nabla^*_\xi T(R\xi) = -\frac{\gamma M}{R}\Theta(R\xi), \tag{2.52}$$

where $T(R\cdot)$ represents the disturbing potential and $\Theta(R\cdot)$ denotes the vertical deflection. The differential equation (2.52) can be solved in a unique way by means of the fundamental solution with respect to the Beltrami operator

$$T(R\xi) = \frac{\gamma M}{R}\int_{\Omega} \Theta(R\eta) \cdot \nabla^*_\eta G\left(\Delta^*; \xi \cdot \eta\right)\, d\omega(\eta), \tag{2.53}$$

where $(\xi,\eta) \mapsto G(\Delta^*;\xi\cdot\eta)$, $1-\xi\cdot\eta \neq 0$, is the fundamental solution of the Beltrami equation on the unit sphere Ω (see, e.g., [11]) given by

$$G(\Delta^*;\xi\cdot\eta) = \frac{1}{4\pi}\ln(1-\xi\cdot\eta) + \frac{1}{4\pi}(1-\ln(2)). \tag{2.54}$$

The identity (2.53) immediately follows from the Third Green Theorem (cf. [15, 22]) for ∇^* on Ω in connection with (2.40). By virtue of the identity

$$\nabla^*_\eta G(\Delta^*;\xi\cdot\eta) = -\frac{\xi-(\xi\cdot\eta)\eta}{4\pi(1-\xi\cdot\eta)}, \quad \xi\neq\eta, \tag{2.55}$$

the integral (2.53) can be written in the form

$$T(R\xi) = \frac{R}{4\pi}\int_\Omega \Theta(R\eta)\cdot g(\Delta^*;\xi,\eta)\; d\omega(\eta), \tag{2.56}$$

where the vector kernel $g(\Delta^*;\xi,\eta),\ \xi\neq\eta$, is given by

$$g(\Delta^*;\xi,\eta) = -\frac{\gamma M}{R^2}\frac{\xi-(\xi\cdot\eta)\eta}{1-\xi\cdot\eta}. \tag{2.57}$$

Again we are confronted with a representation of the disturbing potential T as an improper integral over the sphere Ω_R.

All our settings leading to the disturbing potential on the sphere Ω_R turn out to be improper integrals. As we have shown they have either the singularity behavior of the single-layer kernel S (cf. Eq. (2.49)) or the characteristic logarithmic singularity of the fundamental solution with respect to the Beltrami operator $G(\Delta^*;\cdot,\cdot)$ (cf. (2.54)). Indeed, the fundamental solution and the single-layer kernel are interrelated (see [15]) by the identities

$$S(\xi\cdot\eta) = \sqrt{2}\; e^{-2\pi G(\Delta^*;\xi\cdot\eta)+\frac{1}{2}} \tag{2.58}$$

and

$$G(\Delta^*;\xi\cdot\eta) = -\frac{1}{2\pi}\ln(S(\xi\cdot\eta)) - \frac{1}{4\pi}(1-2\ln(2)). \tag{2.59}$$

Therefore, we are confronted with the remarkable situation that a (Taylor) regularization of the single-layer kernel implies a regularization of the fundamental solution, and vice versa.

2.2. Zooming-in localization of signature bands

Next, we present multiscale representations for the Neumann kernel N (cf. Eq. (2.50)). Note that all modern multiscale approaches have a conception of wavelets as constituting multiscale building blocks in common, which provide a fast and efficient way to decorrelate a given signal data set.

The characterizing properties of the multiscale approach (basis property, decorrelation, and efficient algorithms) are common features of all wavelets and these attributes form the key for a variety of applications (see, e.g., [12, 15, 20]), particularly for signal reconstruction and decomposition, thresholding, data compression, denoising by, e.g., multiscale signal-to-noise ratio, etc. and, in particular, decorrelation.

Next, we follow the (taylorized) regularization methods presented in [23] for linear regularization of the single-layer kernel S and [21] for linear regularization of the fundamental solution $G(\Delta^*;\cdot,\cdot)$ of the Beltrami equation. For higher-order approximations, the reader is referred to the Ph.D.-theses [9] and [73].

The essential idea is to regularize the single-layer kernel function

$$S(t) = \frac{\sqrt{2}}{\sqrt{1-t}} \tag{2.60}$$

by replacing it by a Taylor linearization. To this end, we notice that the first derivative of the kernel S is given by

$$S'(t) = \frac{1}{\sqrt{2}(1-t)^{\frac{3}{2}}}, \qquad t \in [-1,1). \tag{2.61}$$

Consequently, we obtain as (Taylor) linearized approximation corresponding to the expansion point $1-\frac{\tau^2}{2R^2},\ \tau \in (0,2R]$,

$$S(t) = S\left(1-\frac{\tau^2}{2R^2}\right) + S'\left(1-\frac{\tau^2}{2R^2}\right)\left(t-\left(1-\frac{\tau^2}{2R^2}\right)\right) + \cdots. \tag{2.62}$$

In more detail, the kernel S is replaced by its (Taylor) linearized approximation S^τ at the point $1-\frac{\tau^2}{2R^2},\ \tau \in (0,2R]$, given by

$$S^\tau(t) = \begin{cases} \frac{R}{\tau}\left(3-\frac{2R^2}{\tau^2}(1-t)\right), & 0 \le 1-t \le \frac{\tau^2}{2R^2}, \\ \frac{\sqrt{2}}{\sqrt{1-t}}, & \frac{\tau^2}{2R^2} < 1-t \le 2. \end{cases} \tag{2.63}$$

Note that the expansion point $1-\tau^2/(2R^2),\ \tau \in (0,2R]$, is chosen in consistency with the notation in the initial paper [21] and the subsequent papers [14] and [23]. A graphical illustration of the original kernel $S(t)$ and a τ-scale dependent version of its linear space-regularized kernel $S^\tau(t)$ is shown in Figure 2.4.

Clearly, the function S^τ is continuously differentiable on the interval $[-1,1]$, and we have

$$\left(S^\tau\right)'(t) = \begin{cases} \frac{2R^3}{\tau^3}, & 0 \le 1-t \le \frac{\tau^2}{2R^2}, \\ \frac{1}{\sqrt{2}(1-t)^{\frac{3}{2}}}, & \frac{\tau^2}{2R^2} < 1-t \le 2. \end{cases} \tag{2.64}$$

Furthermore, the functions S and S^τ are monotonously increasing on the interval $[-1,1)$, such that $S(t) \ge S^\tau(t) \ge S(-1) = S^\tau(-1) = 1$ holds true on the interval $[-1,1)$. Considering the difference between the kernel S and its linearly regularized version S^τ, we find

$$S(t) - S^\tau(t) = \begin{cases} \frac{\sqrt{2}}{\sqrt{1-t}} - \frac{R}{\tau}\left(3-\frac{2R^2}{\tau^2}(1-t)\right), & 0 < 1-t \le \frac{\tau^2}{2R^2}, \\ 0, & \frac{\tau^2}{2R^2} < 1-t \le 2. \end{cases} \tag{2.65}$$

By elementary manipulations of one-dimensional analysis we readily obtain

$$\int_{-1}^{1} |S(t) - S^\tau(t)|\, dt \;=\; O(\tau). \tag{2.66}$$

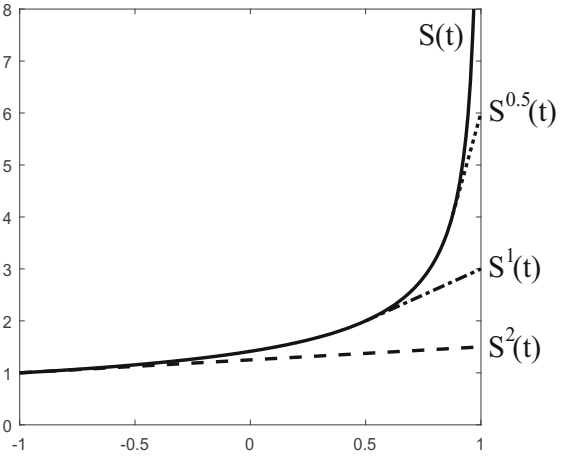

FIGURE 2.4. Single-layer kernel $S(t)$ (continuous black line) and its Taylor linearized regularization $S^\tau(t)$, for $R = 1$ and $\tau = \frac{1}{2}, 1, 2$ (dotted lines).

As a consequence, we have

Lemma 2.5. *For $F \in C^{(0)}(\Omega)$ and S^τ defined by* (2.63) *the limit relation*

$$\lim_{\tau\to 0+} \sup_{\xi\in\Omega} \left| \int_\Omega S(\xi\cdot\eta)F(\eta)\, d\omega(\eta) - \int_\Omega S^\tau(\xi\cdot\eta)(\xi\cdot\eta)F(\eta)\, d\omega(\eta) \right| = 0 \tag{2.67}$$

holds true.

In a similar way, by some elementary calculations, one can find the following relations that are also of importance for the Stokes boundary value problem (see also the Ph.D.-theses [9, 73]).

Lemma 2.6. *Let S be the single-layer kernel given by* (2.60) *and let $S^\tau, \tau \in (0, 2R]$, be the corresponding (Taylor) linearized regularized kernel defined by* (2.63)*. Then*

$$\lim_{\tau\to 0+} \int_{-1}^{1} |\ln(1+S(t)) - \ln(1+S^\tau(t))|\, dt = 0, \tag{2.68}$$

$$\lim_{\tau\to 0+} \int_{-1}^{1} \left| \ln\left(\frac{1}{S(t)} + \frac{1}{(S(t))^2}\right) - \ln\left(\frac{1}{S^\tau(t)} + \frac{1}{(S^\tau(t))^2}\right) \right| dt = 0, \tag{2.69}$$

$$\lim_{\tau\to 0+} \int_{-1}^{1} \left((S(t))^2 - (S^\tau(t))^2 \right) \sqrt{1-t^2}\, dt = 0. \tag{2.70}$$

To study the surface gradient and the surface curl gradient, we let F be of class $C^{(1)}(\Omega)$. Letting $\mathbf{t}_\xi \in \mathbb{R}^{3\times 3}$ be the orthogonal matrix (with $\det(\mathbf{t}_\xi) = 1$) leaving ε^3 fixed such that $\mathbf{t}_\xi \xi = \varepsilon^3$, we get

$$\nabla_\xi^* \int_\Omega S(\xi\cdot\eta)F(\eta)\, d\omega(\eta) = \int_\Omega S(\eta_3)\nabla_\xi^* F(\mathbf{t}_\xi^T\eta)\, d\omega(\eta) \tag{2.71}$$

for $\xi \in \Omega$ and $\eta = (\eta_1, \eta_2, \eta_3)^T$. By regularizing the single-layer kernel, we obtain

$$\int_\Omega \nabla_\xi^* S^\tau(\xi \cdot \eta) F(\eta)\ d\omega(\eta) = \int_\Omega S^\tau(\eta_3) \nabla_\xi^* F(\mathbf{t}_\xi^T \eta)\ d\omega(\eta) \tag{2.72}$$

for $\xi \in \Omega$. The same argumentation holds true for the operator L^*. Therefore, Lemma 2.5 leads us to the following limit relations (see [22]).

Lemma 2.7. *Let F be of class $C^{(1)}(\Omega)$. Let S^τ be given by* (2.63)*. Then*

$$\lim_{\tau \to 0+} \sup_{\xi \in \Omega} \left| \int_\Omega \nabla_\xi^* S^\tau(\xi \cdot \eta) F(\eta) d\omega(\eta) - \nabla_\xi^* \int_\Omega S(\xi \cdot \eta) F(\eta) d\omega(\eta) \right| = 0, \tag{2.73}$$

$$\lim_{\tau \to 0+} \sup_{\xi \in \Omega} \left| \int_\Omega \mathrm{L}_\xi^* S^\tau(\xi \cdot \eta) F(\eta) d\omega(\eta) - \mathrm{L}_\xi^* \int_\Omega S(\xi \cdot \eta) F(\eta) d\omega(\eta) \right| = 0. \tag{2.74}$$

Using the kernel $G^\tau(\Delta^*; \cdot)$, given by (see Eq. (2.59))

$$G^\tau(\Delta^*; t) = -\frac{1}{2\pi} \ln(S^\tau(t)) - \frac{1}{4\pi}(1 - 2\ln(2)), \quad -1 \le t \le 1, \tag{2.75}$$

as *"single-layer kernel regularization" of the fundamental solution* $G(\Delta^*; \cdot)$, we are led to the following integral relations.

Lemma 2.8. *For $F \in C^{(0)}(\Omega)$ and $G^\tau(\Delta^*; \cdot)$ defined by* (2.75)*, we have*

$$\lim_{\tau \to 0+} \sup_{\xi \in \Omega} \left| \int_\Omega G(\Delta^*; \xi \cdot \eta) F(\eta)\ d\omega(\eta) - \int_\Omega G^\tau(\Delta^*; \xi \cdot \eta) F(\eta)\ d\omega(\eta) \right| = 0, \tag{2.76}$$

and

$$\lim_{\tau \to 0+} \sup_{\xi \in \Omega} \left| \int_\Omega \nabla_\xi^* G^\tau(\Delta^*; \xi \cdot \eta) F(\eta)\ d\omega(\eta) - \nabla_\xi^* \int_\Omega G(\Delta^*; \xi \cdot \eta) F(\eta)\ d\omega(\eta) \right| = 0, \tag{2.77}$$

$$\lim_{\tau \to 0+} \sup_{\xi \in \Omega} \left| \int_\Omega \mathrm{L}_\xi^* G^\tau(\Delta^*; \xi \cdot \eta) F(\eta)\ d\omega(\eta) - \mathrm{L}_\xi^* \int_\Omega G(\Delta^*; \xi \cdot \eta) F(\eta)\ d\omega(\eta) \right| = 0. \tag{2.78}$$

Remark 2.9. Numerical implementations and computational aspects of the Taylor regularization techniques as presented here have been applied (even for subsets of Ω_R) to different fields of physical geodesy (see, e.g., [13–15, 21–23] and the references therein).

The regularization techniques enable us to formulate multiscale solutions for the disturbing potential from gravity disturbances or vertical deflections (note that we need higher-order regularizations whenever gravitational observables containing second or higher-order derivatives come into play; an example is gravity gradiometry, which will not be discussed here).

As point of departure for our considerations serves the special case study of the linear regularization of the single-layer kernel in the integral representation of the solution of the Neumann boundary-value problem (ENPPG).

Disturbing Potential from Gravity Disturbances. As we already know, the solution of the (Earth's) disturbing potential $T \in Pot^{(1)}\left(\mathbb{R}^3 \backslash \mathcal{B}_R(0)\right)$ from known vertical

derivatives, i.e., gravity disturbances $D = \frac{\partial T}{\partial \nu}\big|_{\Omega_R}$, satisfying the conditions (2.40) on the sphere Ω_R, can be formulated as an improper integral (see Eq. (2.51))

$$T(R\xi) = \frac{R}{4\pi} \int\limits_{\Omega} D(R\eta)\ N(\xi \cdot \eta)\, d\omega(\eta),\ \xi \in \Omega, \tag{2.79}$$

with the Neumann kernel N (cf. (2.50)). Our interest is to formulate regularizations of the disturbing potential T by use of the (Taylor) linearized approximation of the singe-layer kernel $S^\tau : [-1,1] \to \mathbb{R},\ \tau \in (0, 2R]$, introduced in (2.63). As a result, we obtain the regularized Neumann kernels

$$\begin{aligned} N^\tau(\xi \cdot \eta) &= \begin{cases} S^\tau(\xi \cdot \eta) - \ln\left(1 + S^\tau(\xi \cdot \eta)\right), & 0 \le 1 - \xi \cdot \eta \le \frac{\tau^2}{2R^2}, \\ S(\xi \cdot \eta) - \ln(1 + S(\xi \cdot \eta)), & \frac{\tau^2}{2R^2} < 1 - \xi \cdot \eta \le 2, \end{cases} \\ &= \begin{cases} \frac{R}{\tau}\left(3 - \frac{2R^2}{\tau^2}(1 - \xi \cdot \eta)\right) - \ln\left(1 + \frac{R}{\tau}\left(3 - \frac{2R^2}{\tau^2}(1 - \xi \cdot \eta)\right)\right), & \\ \qquad\qquad 0 \le 1 - \xi \cdot \eta \le \frac{\tau^2}{2R^2}, & \\ \frac{\sqrt{2}}{\sqrt{1 - \xi \cdot \eta}} - \ln\left(1 + \frac{\sqrt{2}}{\sqrt{1 - \xi \cdot \eta}}\right), & \frac{\tau^2}{2R^2} < 1 - \xi \cdot \eta \le 2. \end{cases} \end{aligned} \tag{2.80}$$

In doing so, we are immediately led to the regularized representation of the disturbing potential T corresponding to the known gravity disturbances:

$$\begin{aligned} T^\tau(R\xi) &= \frac{R}{4\pi} \int\limits_{\eta \in \Omega} D(R\eta) N^\tau(\xi \cdot \eta)\, d\omega(\eta) \qquad (2.81) \\ &= \frac{R}{4\pi} \int\limits_{\substack{\eta \in \Omega; \\ 1 - \xi \cdot \eta > \frac{\tau^2}{2R^2}}} D(R\eta) N(\xi \cdot \eta)\, d\omega(\eta) + \frac{R}{4\pi} \int\limits_{\substack{\eta \in \Omega; \\ 1 - \xi \cdot \eta \le \frac{\tau^2}{2R^2}}} D(R\eta) N^\tau(\xi \cdot \eta)\, d\omega(\eta). \end{aligned}$$

The representation (2.81) is remarkable, since the integrands of T and T^τ only differ on the spherical cap

$$\Gamma_{\tau^2/(2R^2)}(\xi) = \left\{ \eta \in \Omega\ :\ 1 - \xi \cdot \eta \le \frac{\tau^2}{2R^2} \right\}. \tag{2.82}$$

By aid of Lemma 2.5 and Lemma 2.6, we obtain

Theorem 2.10. *Suppose that T is the solution of the Neumann boundary-value problem* (ENPPG) *of the form* (2.79). *Let T^τ, $\tau \in (0, 2R]$, represent its regularization* (2.81). *Then*

$$\lim_{\tau \to 0+} \sup_{\xi \in \Omega} |T(R\xi) - T^\tau(R\xi)| = 0. \tag{2.83}$$

For numerical applications, we have to go over to scale-discretized approximations of the solution to the boundary-value problem (ENPPG). For that purpose, we choose a monotonously decreasing sequence $\{\tau_j\}_{j \in \mathbb{N}_0}$, such that

$$\lim_{j \to \infty} \tau_j = 0,\ \tau_0 = 2R. \tag{2.84}$$

A particularly important example, that we use in our numerical implementations below, is the dyadic sequence with

$$\tau_j = 2^{1-j}R, \quad j \in \mathbb{N}_0. \tag{2.85}$$

It is easy to see that $2\tau_{j+1} = \tau_j$, $j \in \mathbb{N}_0$, is the relation between two consecutive elements of the sequence. In correspondence to the sequence $\{\tau_j\}_{j\in\mathbb{N}_0}$, a sequence $\{N^{\tau_j}\}_{j\in\mathbb{N}_0}$ of discrete versions of the regularized Neumann kernels (2.80), so-called *Neumann scaling functions*, is available. Figure 2.5 (left) shows a graphical illustration of the regularized Neumann kernels for different scales j.

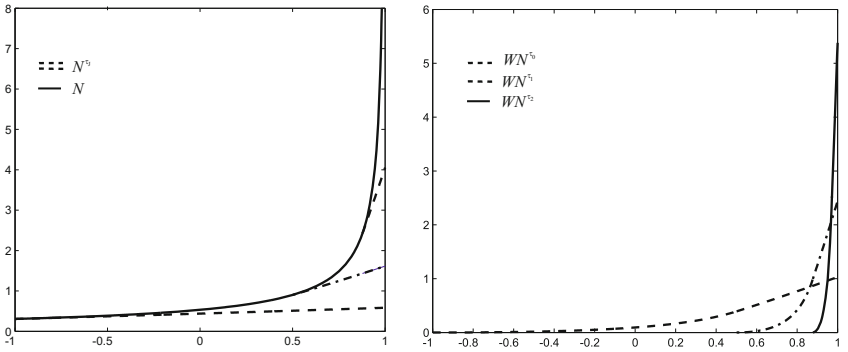

FIGURE 2.5. Illustration of the Neumann kernel $N(t)$ (left, continuous black line) and its Taylor linearized regularization $N^{\tau_j}(t)$, $j = 0, 1, 2$, $\tau_j = 2^{1-j}R$ and $R = 1$ (left, dotted lines). The corresponding Taylor linearized Neumann wavelets $WN^{\tau_j}(t)$ for scales $j = 0, 1, 2$, are shown on the right.

The *regularized Neumann wavelets*, forming the sequence $\{WN^{\tau_j}\}_{j\in\mathbb{N}_0}$, are understood to be the difference of two consecutive regularized Neumann scaling functions, respectively,

$$WN^{\tau_j} = N^{\tau_{j+1}} - N^{\tau_j}, \quad j \in \mathbb{N}_0. \tag{2.86}$$

The Neumann wavelets are illustrated in Figure 2.5 (right). These wavelets possess the numerically important property of a local support. More concretely, $\eta \mapsto WN^{\tau_j}(\xi\cdot\eta)$, $\eta \in \Omega$, vanishes everywhere outside the spherical cap $\Gamma_{\tau_j^2/(2R^2)}(\xi)$.

Let $J \in \mathbb{N}_0$ be an arbitrary scale. Suppose that N^{τ_J} is the regularized Neumann scaling function at scale J. Furthermore, let WN^{τ_j}, $j = 0, \ldots, J$, be the regularized Neumann wavelets as given by (2.86). Then, we obviously have

$$N^{\tau_J} = N^{\tau_0} + \sum_{j=0}^{J-1} WN^{\tau_j}. \tag{2.87}$$

The local support of the Neumann wavelets within the framework of (2.87) should be studied in more detail: We start with the globally supported scaling kernel $N^{\tau_0} = N^{2R}$. Then we add more and more wavelet kernels WN^{τ_j}, $j = 0, \ldots, J-1$,

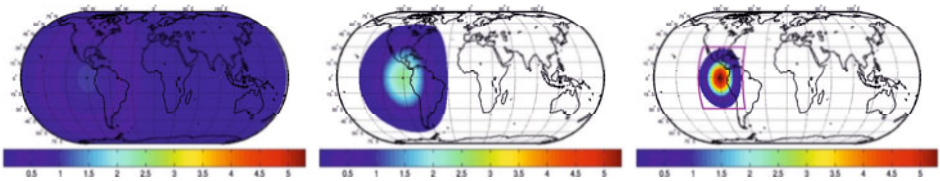

(a) scale $j = 0$ (b) $j = 1$ (c) $j = 2$

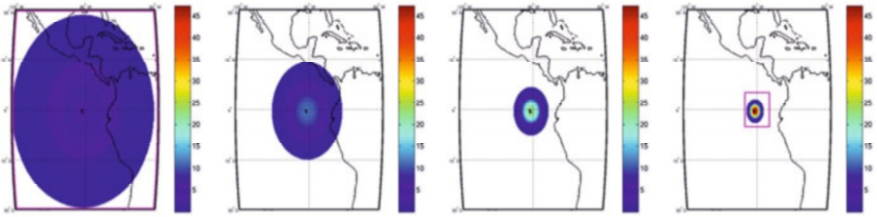

(d) $j = 2$ (e) $j = 3$ (f) $j = 4$ (g) $j = 5$

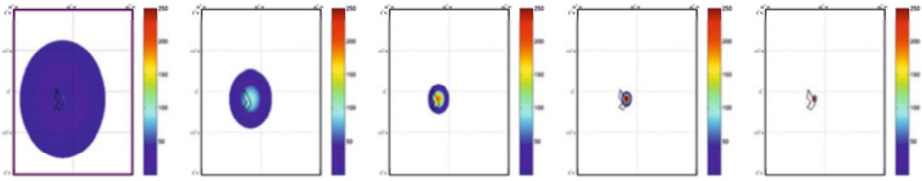

(h) $j = 5$ (i) $j = 6$ (j) $j = 7$ (k) $j = 8$ (l) $j = 9$

FIGURE 2.6. Illustration of the regularized Neumann wavelets $\eta \mapsto WN^{\tau_j}(\xi \cdot \eta)$ for scales $j = 0, \ldots, 9$ to visualize the local supports $\Gamma_{\tau_j^2/(2R^2)}(\xi)$ for a fixed ξ (cf. [73]) "zooming in" to the hotspot of the Galapagos islands.

to achieve the scaling kernel N^{τ_J}. It is of particular importance that the kernel functions $\eta \mapsto WN^{\tau_j}(\xi \cdot \eta)$, $\xi \in \Omega$ fixed, are ξ-zonal functions with local support (spherical caps). Figure 2.6 illustrates the computationally relevant regions for the different wavelet scales j (more detailed studies are presented in the Ph.D. theses [9, 73]). For a better understanding, the areas outside the caps are chosen to be uncolored. Clearly, the support of the wavelets WN^{τ_j} becomes more localized for increasing scales j. In conclusion, a calculation of an integral representation for the disturbing potential T starts with a global trend approximation using the scaling kernel at scale $j = 0$ (of course, this requires data on the whole sphere, but the data can be rather sparsely distributed since they only serve as a trend approximation). Step by step, we are able to refine this approximation by use of wavelets of increasing scale. The spatial localization of the wavelets successively allows a better spatial resolution of the disturbing potential T. Additionally, the local supports of the wavelets provide a computational advantage since the integration has to be performed on smaller and smaller spherical caps. In consequence,

the presented numerical technique becomes capable of handling heterogeneously distributed data.

All in all, keeping the space-localizing property of the regularized Neumann scaling and wavelet functions in mind, we are able to establish an approximation of the solution of the disturbing potential T from gravity disturbances D in form of a "zooming-in" multiscale method. A low-pass filtered version of the disturbing potential T at the scale j in an integral representation over the unit sphere Ω is given by (compare Eq. (2.81))

$$T^{\tau_j}(R\xi) = \frac{R}{4\pi} \int_{\Omega} D(R\eta)\; N^{\tau_j}(\xi \cdot \eta)\, d\omega(\eta), \qquad \xi \in \Omega, \tag{2.88}$$

while the j-scale band-pass filtered version of T leads to the integral representation by use of the wavelets

$$WT^{\tau_j}(R\xi) = \frac{R}{4\pi} \int\limits_{\Gamma_{\tau_j^2/(2R^2)}(\xi)} D(R\eta)\; WN^{\tau_j}(\xi \cdot \eta)\, d\omega(\eta), \qquad \xi \in \Omega. \tag{2.89}$$

Theorem 2.11. *Let $T^{\tau_{J_0}}$ be the regularized version of the disturbing potential at some arbitrary initial scale J_0 as given in* (2.88)*, and let $WT^{\tau_{J_0+j}}$, $j = 0, 1, \ldots$, be given by* (2.89)*. Then, the following reconstruction formula holds true:*

$$\lim_{N\to\infty} \sup_{\xi\in\Omega} \left| T(R\xi) - \left(T^{\tau_{J_0}}(R\xi) + \sum\nolimits_{j=0}^{N} WT^{\tau_{J_0+j}}(R\xi) \right) \right| = 0.$$

The multiscale procedure (*wavelet reconstruction*) as developed here can be illustrated by the following scheme

$$\begin{array}{ccccccccc} WT^{\tau_{J_0}} & & & & WT^{\tau_{J_0+1}} & & & & \\ & \searrow & & & & \searrow & & & \\ T^{\tau_{J_0}} & \longrightarrow & + & \longrightarrow & T^{\tau_{J_0+1}} & \longrightarrow & + & \longrightarrow & T^{\tau_{J_0+2}} \ \ldots \ . \end{array}$$

As a consequence, a tree algorithm based on the regularization in the space domain has been realized for determining the disturbing potential T from locally available data sets of gravity disturbances D. An example is shown in Figure 2.7 (following [73]).

In order to get a fully discretized solution of the Neumann boundary-value problem (ENPPG), approximate integration by use of appropriate cubature formulas is necessary (see, e.g., [16, 35] for more details about approximate integration on the (unit) sphere). The fully discretized multiscale approximations have the following representations

$$T^{\tau_j}(R\xi) \simeq \frac{R}{4\pi} \sum_{k=1}^{N_j} w_k^{N_j} D\left(R\eta_k^{N_j}\right)\; N^{\tau_j}\left(\xi \cdot \eta_k^{N_j}\right), \quad \xi \in \Omega, \tag{2.90}$$

$$WT^{\tau_j}(R\xi) \simeq \frac{R}{4\pi} \sum_{k=1}^{N_j} w_k^{N_j} D\left(R\eta_k^{N_j}\right)\; WN^{\tau_j}\left(\xi \cdot \eta_k^{N_j}\right), \quad \xi \in \Omega, \tag{2.91}$$

where $\eta_k^{N_j}$ are the N_j integration knots and $w_k^{N_j}$ the integration weights.

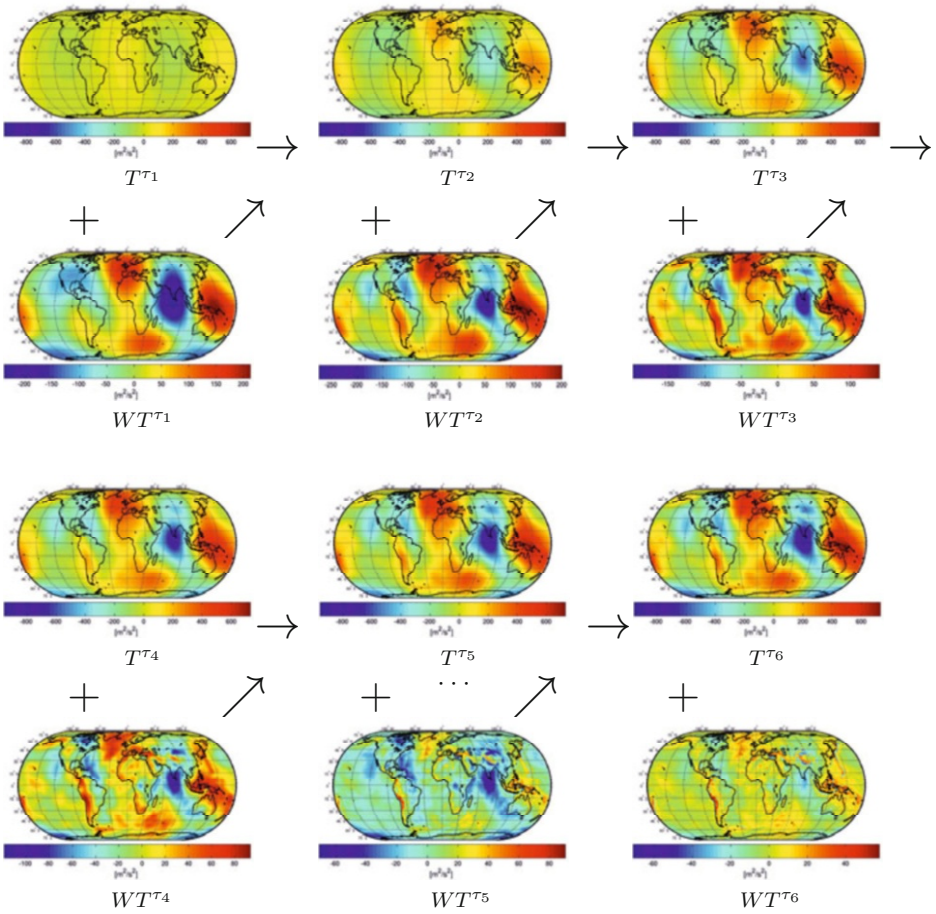

FIGURE 2.7. Illustration of a (global) multiscale approximation of the Earth's disturbing potential T in $[\frac{m^2}{s^2}]$ from gravity disturbances D, i.e., low-pass filtered versions T^{τ_j} and detail information (band-pass filtered versions) WT^{τ_j} for scales $j = 1, \ldots, 6$, by use of the linear Neumann scaling functions and wavelets computed from 4 000 000 data points distributed over the whole sphere Ω_R (from the Ph.D.-thesis [73], Geomathematics Group, University of Kaiserslautern).

Whereas the sum in (2.90) has to be calculated on the whole sphere Ω, the summation in (2.91) has to be computed only for the local supports of the wavelets (note that the symbol $\simeq$ means that the error between the right-hand and the left-hand side can be neglected).

Figures 2.8 to 2.10 present a decomposition of the Earth's disturbing potential T in low-pass and band-pass filtered parts for data sets of increasing data density.

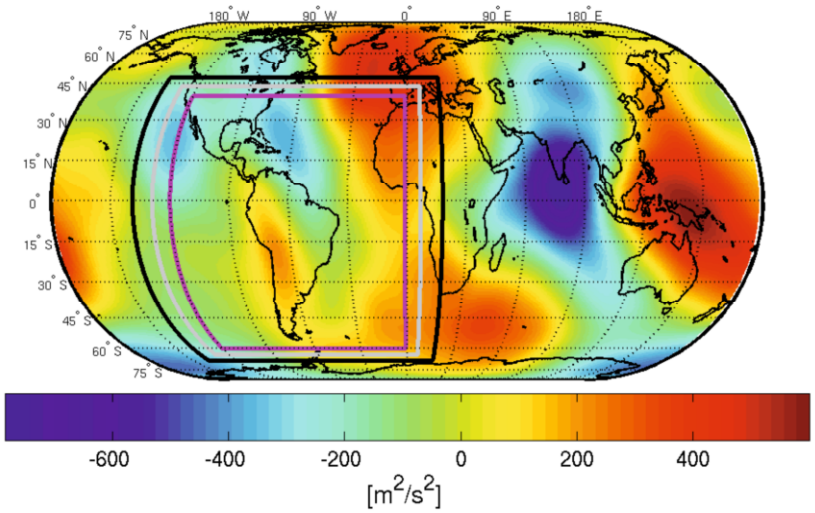

(a) Low pass part T^{τ_4} calculated from 490 000 data points distributed over the whole sphere Ω_R

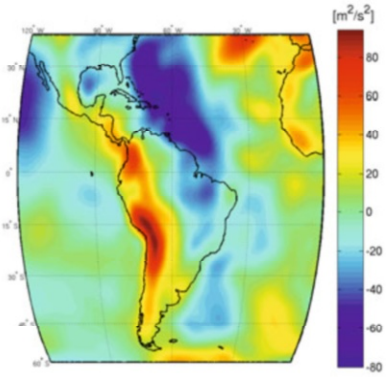

(b) Details WT^{τ_4} at scale 4 from 281 428 data points distributed within the black bordered region in Figure 2.8(a)

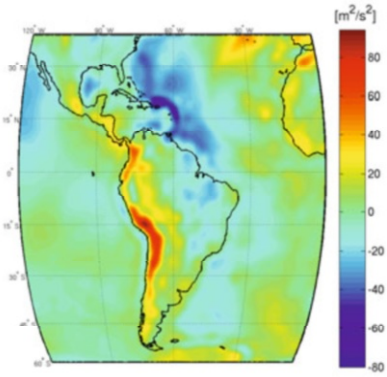

(c) Details WT^{τ_5} at scale 5 from 226 800 data points distributed within the gray bordered region in Figure 2.8(a)

FIGURE 2.8. Low-pass filtered version T^{τ_4} of the disturbing potential T in $[\frac{m^2}{s^2}]$ and the corresponding band-pass filtered versions WT^{τ_j} for scales $j = 4, 5$ of the magenta bordered region in subfigure 2.8(a) calculated from different numbers of data points (from the Ph.D.-thesis [73], Geomathematics Group, University of Kaiserslautern).

Seen from the geodetic reality, the figures are remarkable in the following sense: For getting a better accuracy in numerical integration procedures providing the

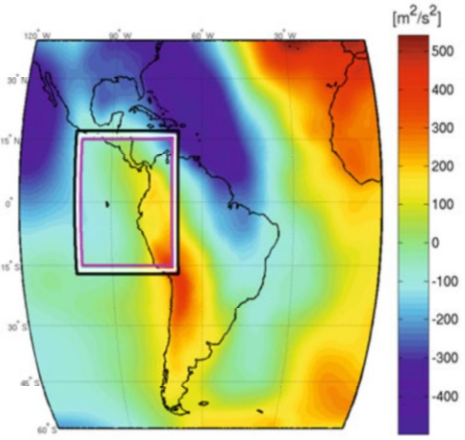

(a) Low pass part T^{τ_6} of the magenta bordered region in Figure 2.8(a) computed by the sum of T^{τ_4} (Figure 2.8(a)), WT^{τ_4} (Figure 2.8(b)), and WT^{τ_5} (Figure 2.8(c)) in this region

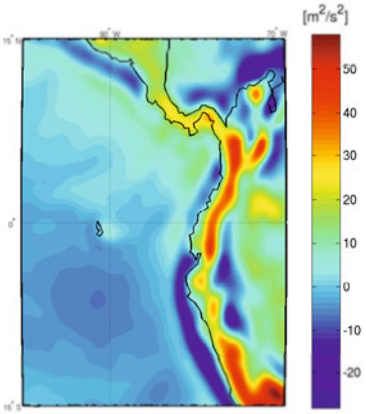

(b) Details WT^{τ_6} at scale 6 from 71 253 data points distributed within the black bordered region in Figure 2.9(a)

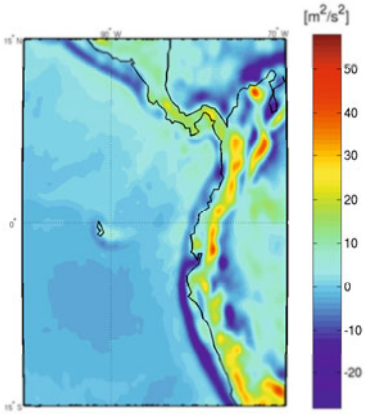

(c) Details WT^{τ_7} at scale 7 from 63 190 data points distributed within the gray bordered region in Figure 2.9(a)

FIGURE 2.9. Low-pass filtered version T^{τ_6} of the disturbing potential T in $[\frac{m^2}{s^2}]$ of the magenta bordered region in subfigure 2.8(a) and the corresponding band-pass filtered versions WT^{τ_j} for scales $j = 6, 7$ (from the Ph.D.-thesis [73], Geomathematics Group, University of Kaiserslautern).

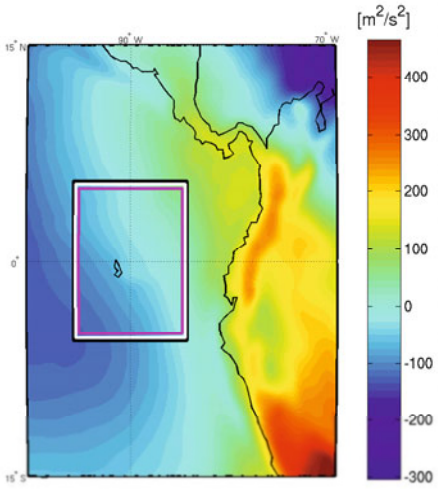

(a) Low pass part T^{τ_8} of the magenta bordered region in Figure 2.9(a) computed by the sum of T^{τ_6} (Figure 2.9(a)), WT^{τ_6} (Figure 2.9(b)), and WT^{τ_7} (Figure 2.9(c)) in this region

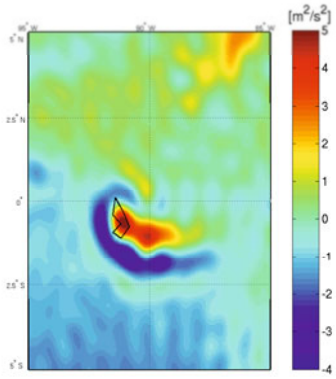

(b) Details WT^{τ_8} at scale 8 from 71 253 data points distributed within the black bordered region in Figure 2.10(a)

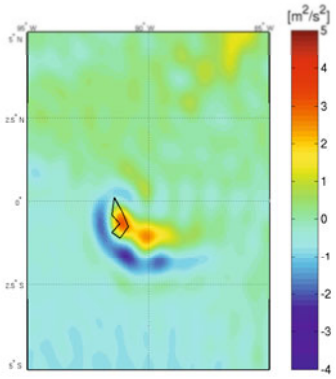

(c) Details WT^{τ_9} at scale 9 from 63 190 data points distributed within the gray bordered region in Figure 2.10(a)

FIGURE 2.10. Low-pass filtered version T^{τ_8} of the disturbing potential T in $[\frac{m^2}{s^2}]$ of the magenta bordered region in subfigure 2.9(a) and the corresponding band-pass filtered versions WT^{τ_j} for scales $j = 8, 9$ (from the Ph.D.-thesis [73], Geomathematics Group, University of Kaiserslautern).

(global) solution of the boundary-value problem (ENPPG) as illustrated in Figure 2.8 (a), we need denser, globally over the whole sphere Ω_R equidistributed data sets (most notably, in the sense of Weyl's Law of Equidistribution). However, in today's reality of gravitational field observation, we are confronted with the problem that terrestrial gravitational data (such as gravity disturbances, gravity anomalies) of sufficient width and quality are only available for certain parts of the Earth's surface (for more details concerning the observational aspects see, e.g., [6–8, 61, 62]). As a matter of fact, there are large gaps, particularly at sea, where no data sets of sufficient quality are available at all. This is the reason why the observational situation implies the need for specific geodetically oriented modeling techniques taking the heterogeneous data situation and the local availability of the data (usually related to latitude-longitude data grids) into consideration. In this respect, the "zooming-in" realization based on single-layer space-regularization is a suitable efficient and economic mathematical answer.

Disturbing Potential from Vertical Deflections. As already known from (2.56), the solution of the surface differential equation (see Eq. (2.36))

$$\nabla_\xi^* T(R\xi) = -\frac{\gamma M}{R}\Theta(R\xi), \qquad \xi \in \Omega, \tag{2.92}$$

determining the disturbing potential T from prescribed vertical deflections Θ under the conditions (2.40) is given by

$$T(R\xi) = \frac{R}{4\pi}\int_\Omega \Theta(R\eta)\cdot g\left(\Delta^*;\xi,\eta\right)\, d\omega(\eta), \tag{2.93}$$

where the vector kernel $g\left(\Delta^*;\xi,\eta\right),\ 1-\xi\cdot\eta>0$, reads as follows (see Eq. (2.57))

$$\begin{aligned} g\left(\Delta^*;\xi,\eta\right) &= -\frac{1}{2}\frac{\gamma M}{R^2}\frac{2}{1-\xi\cdot\eta}(\xi-(\xi\cdot\eta)\eta) \\ &= -\frac{1}{2}\frac{\gamma M}{R^2}(S(\xi\cdot\eta))^2(\xi-(\xi\cdot\eta)\eta). \end{aligned} \tag{2.94}$$

Analogously to the calculation of the disturbing potential T from known gravity disturbances D (i.e., the Neumann problem (ENPPG)), the numerical calamities of the improper integral in (2.93) can be circumvented by replacing the zonal kernel $S(\xi\cdot\eta)$ by the regularized kernel $S^\tau(\xi\cdot\eta)$. This process leads to space-regularized representations T^τ of the disturbing potential T calculated from vertical deflections Θ within a multiscale "zooming-in" procedure analogous to the approach for gravity disturbances as input data. To be more concrete, the kernel function $g(\Delta^*;\cdot,\cdot)$ is replaced by the space-regularized function using Eq. (2.63)

$$g^\tau\left(\Delta^*;\xi,\eta\right) = -\frac{\gamma M}{2R^2}\left(S^\tau(\xi\cdot\eta)\right)^2(\xi-(\xi\cdot\eta)\eta), \tag{2.95}$$

$$= \begin{cases} -\frac{\gamma M}{2R^2}\left(\frac{9R^2}{\tau^2}-\frac{12R^4}{\tau^4}(1-\xi\cdot\eta)+\frac{4R^6}{\tau^6}(1-\xi\cdot\eta)^2\right)(\xi-(\xi\cdot\eta)\eta), & 0\le 1-\xi\cdot\eta\le\frac{\tau^2}{2R^2}, \\ -\frac{\gamma M}{2R^2}\frac{2}{1-\xi\cdot\eta}(\xi-(\xi\cdot\eta)\eta), & \frac{\tau^2}{2R^2}<1-\xi\cdot\eta\le 2, \end{cases}$$

for $\tau \in (0, 2R]$. This leads to the following approximative representation of the disturbing potential T:

$$T^{\tau}(R\xi) = \frac{R}{4\pi} \int_{\Omega} \Theta(R\eta) \cdot g^{\tau}\left(\Delta^*; \xi, \eta\right) \, d\omega(\eta), \tag{2.96}$$

with $g^{\tau}(\Delta^*; \cdot, \cdot)$ given by (2.95). Using Eq. (2.70) from Lemma 2.6 we obtain

Theorem 2.12. *Suppose that T is the solution* (2.93) *of the differential equation* (2.92)*, with Θ being a member of the class of continuous vector-valued functions $c^{(0)}(\Omega_R)$. Let T^{τ}, $\tau \in (0, 2R]$, represent its regularized solution of the form* (2.96)*. Then*

$$\lim_{\tau \to 0+} \sup_{\xi \in \Omega} |T(R\xi) - T^{\tau}(R\xi)| = 0. \tag{2.97}$$

By restricting $\{g^{\tau}\left(\Delta^*; \cdot, \cdot\right)\}_{\tau \in (0, 2R]}$ to the sequence $\{g^{\tau_j}\left(\Delta^*; \cdot, \cdot\right)\}_{j \in \mathbb{N}_0}$, corresponding to a set of scaling parameters $\{\tau_j\}_{j \in \mathbb{N}_0}$ satisfying $\tau_j \in (0, 2R]$ and $\lim_{j \to \infty} \tau_j = 0$, we are canonically led to regularized vector scaling functions such that a scale-discrete solution method for the differential equation (2.92) can be formulated. The vector scaling function $g^{\tau_{j+1}}(\Delta^*; \cdot, \cdot)$ at scale $j + 1$ is constituted by the sum of the vector scaling function $g^{\tau_j}(\Delta^*; \cdot, \cdot)$ and the corresponding discretized vector wavelet $wg^{\tau_j}(\Delta^*; \cdot, \cdot)$, given by

$$wg^{\tau_j}\left(\Delta^*; \xi, \eta\right) = g^{\tau_{j+1}}\left(\Delta^*; \xi, \eta\right) - g^{\tau_j}\left(\Delta^*; \xi, \eta\right). \tag{2.98}$$

Note that (cf. [15])

$$WT^{\tau_j}(R\xi) = \int_{\Omega} \Theta(R\eta) \cdot wg^{\tau_j}(\Delta^*; \xi, \eta) d\omega(\eta).$$

Application: Gravitational signatures of mantle plumes

Galapagos: "The Galapagos hotspot (Figures 2.8–2.10) is a volcanic hotspot in the East Pacific Ocean responsible for the creation of the Galapagos Islands as well as three major aseismic ridge systems, Carnegie, Cocos and Malpelso which are on two tectonic plates. The hotspot is located near the Equator on the Nazca Plate not far from the divergent plate boundary with the Cocos Plate. The tectonic setting of the hotspot is complicated by the Galapagos Triple Junction of the Nazca and Cocos plates with the Pacific Plate. The movement of the plates over the hotspot is determined not solely by the spreading along the ridge but also by the relative motion between the Pacific Plate and the Cocos and Nazca Plates.

The hotspot is believed to be over 20 million years old and in that time, there has been interaction between the hotspot, both of these plates, and the divergent plate boundary, at the Galapagos Spreading Center. Lavas from the hotspot do not exhibit the homogeneous nature of many hotspots; instead there is evidence of four major reservoirs feeding the hotspot. These mix to varying degrees at different locations on the archipelago and also within the Galapagos Spreading Center." (from [71]) (for more details the reader is referred, e.g., to [31] and the references therein).

Hawaii: [58] believe that a stationary mantle plume located beneath the Hawaiian Islands created the Hawaii-Emperor seamount chain while the oceanic lithosphere continuously passed over it. The Hawaii-Emperor chain consists of about 100 volcanic islands, atolls, and seamounts that spread nearly 6000km from the active volcanic island of Hawaii to the 75–80 million year old Emperor seamounts nearby the Aleutian trench. With moving further south east along the island chain, the geological age decreases. The interesting area is the relatively young southeastern part of the chain, situated on the Hawaiian swell, a 1200km broad anomalously shallow region of the ocean floor, extending from the island of Hawaii to the Midway atoll. Here, a distinct gravity disturbance and geoid anomaly occurs that has its maximum around the youngest island that coincides with the maximum topography and both decrease in northwestern direction. The progressive decrease in terms of the geological age is believed to result from the continuous motion of the underlying plate (cf. [50, 72]).

With seismic tomography, several features of the Hawaiian mantle plume are gained (cf. [58] and the references therein). They result in a *Low Velocity Zone* (LVZ) beneath the lithosphere, starting at a depth of about 130–140km beneath the central part of the island of Hawaii. So far, plumes have just been identified as low seismic velocity anomalies in the upper mantle and the transition zone, which is a fairly new achievement. As plumes are relatively thin with respect to their diameter, they are hard to detect in global tomography models. Hence, despite novel advances, there is still no general agreement on the fundamental questions concerning mantle plumes, like their depth of origin, their morphology, their longevity, and even their existence is still discussed controversial. This is due to the fact that many geophysical as well as geochemical observations can be explained by different plume models and even by models that do not include plumes at all (e.g., [10]). With our space-localized multiscale method of deriving gravitational signatures (more concretely, the disturbing potential) from the vertical deflections, we add a new component in specifying essential features of plumes. The vertical deflections of the plume in the region of Hawaii are visualized in Figure 2.11.

From the band-pass filtered detail approximation of the vertical deflections (Figure 2.12) and the corresponding disturbing potential (Figure 2.13), we are able to conclude that the Hawaii plume has an oblique layer structure. As can be seen in the lower scale (for which numerical evidence suggests that they reflect the higher depths), the strongest signal is located in the ocean in a westward direction of Hawaii. With increasing scale, i.e., lower depths, it moves more and more to the Big Island of Hawaii, i.e., in eastward direction.

Iceland: The plume beneath Iceland is a typical example of a ridge-centered mantle plume. An interaction between the North Atlantic ridge and the mantle plume is believed to be the reason for the existence of Iceland, resulting in melt production and crust generation since the continental break-up in the late Palaeocene and early Eocene. Nevertheless, there is still no agreement on the location of the plume before rifting started in the East. Controversial discussions, whether it was

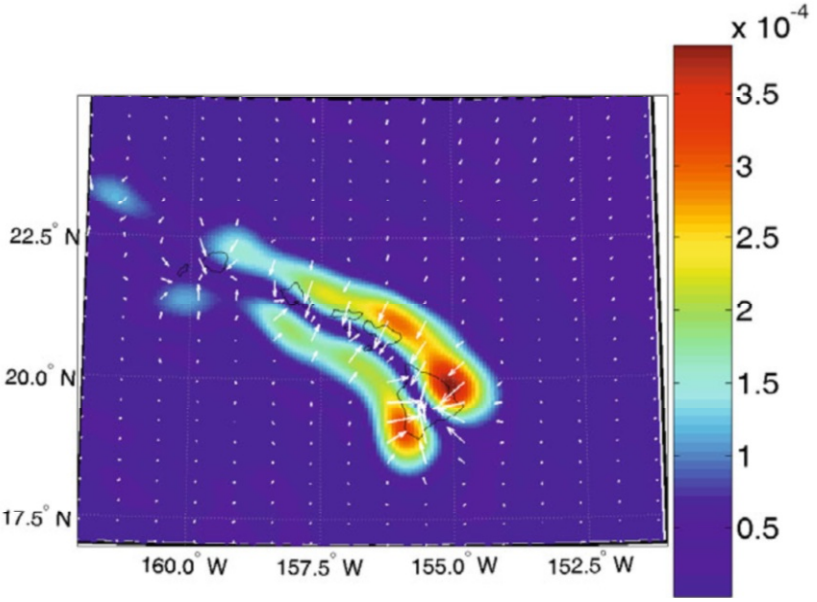

FIGURE 2.11. Illustration of the vertical deflections Θ in the region of Hawaii (from the Ph.D.-thesis [9], Geomathematics Group, University of Kaiserslautern).

located under central or eastern Greenland about 62-64 million years ago are still in progress (cf. [63] and the references therein).

Iceland itself represents the top of a nearly circular rise topography, with a maximum of about 2.8km above the surrounding seafloor in the south of the glacier "Vatnajökull". Beneath this glacier, several active volcanoes are located, which are supposed to be fed by a mantle plume. The surrounding oceanic crust consists of three different types involving a crust thickness that is more than three times as thick as average oceanic crusts. Seismic tomography provides evidence of the existence of a mantle plume beneath Iceland, resulting in low velocity zones in the upper mantle and the transition zone, but also hints for anomalies in the deeper mantle seem to exist. The low velocity anomalies have been detected in depths ranging from at least 400km up to about 150km. Above 150km, ambiguous seismic-velocity structures were obtained involving regions of low velocities covered by regions of high seismic velocities. For a deeper access into the theory of the Iceland plume, the interested reader is referred to [58] and the references therein.

From Figures 2.14 to 2.16, it can be seen that the mantle plume in lower scales, i.e., in higher depths, starts in the North of Iceland and with increasing scale, i.e., lower depths, it moves to the South. It is remarkable that from scale 13 on, the plume seems to divide into two sectors. Since it is known that the disturbing

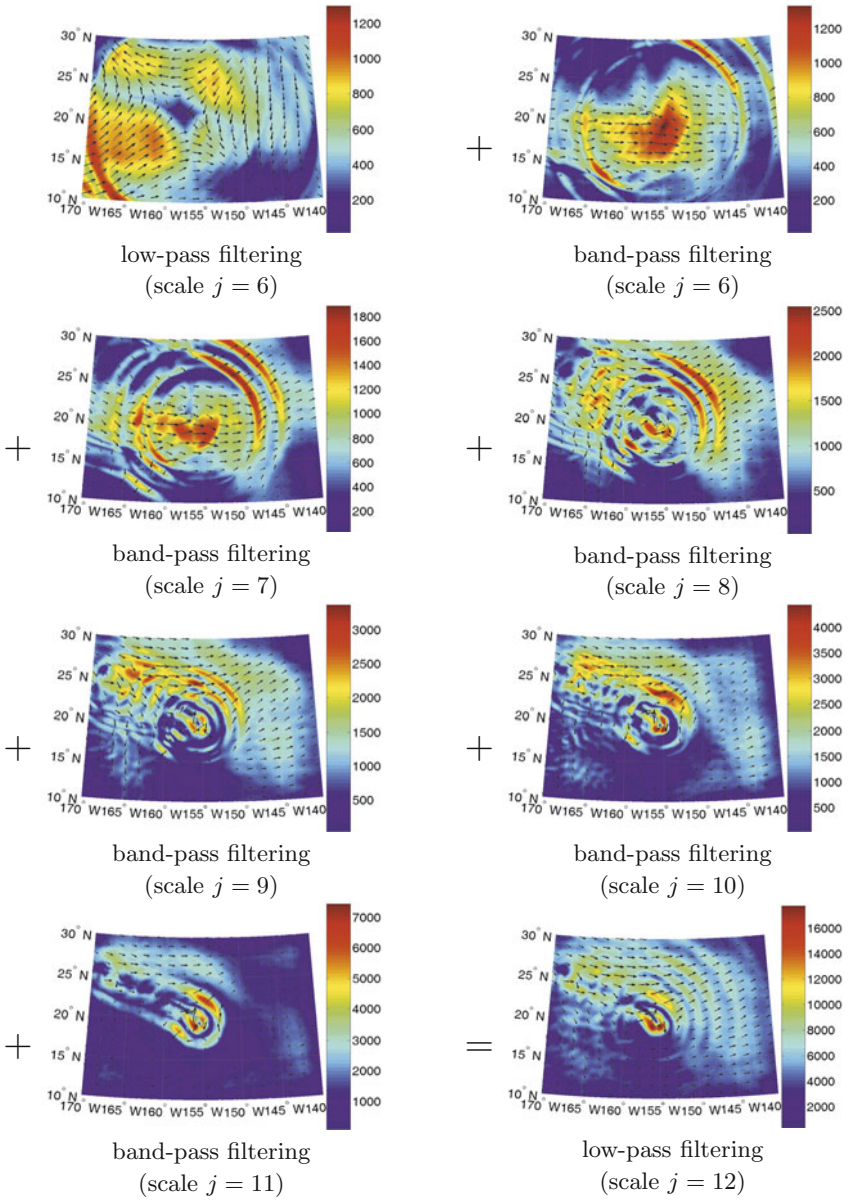

FIGURE 2.12. Approximation of the vector-valued vertical deflections Θ in $[\mathrm{ms}^{-2}]$ of the region of Hawaii (compare Fig. 2.11). A rough low-pass filtering at scale 6 is improved by several band-pass filters of scale $j = 6, \ldots, 11$, the last picture shows the multiscale approximation at scale $j = 12$, (from the Ph.D.-thesis [9], Geomathematics Group, University of Kaiserslautern).

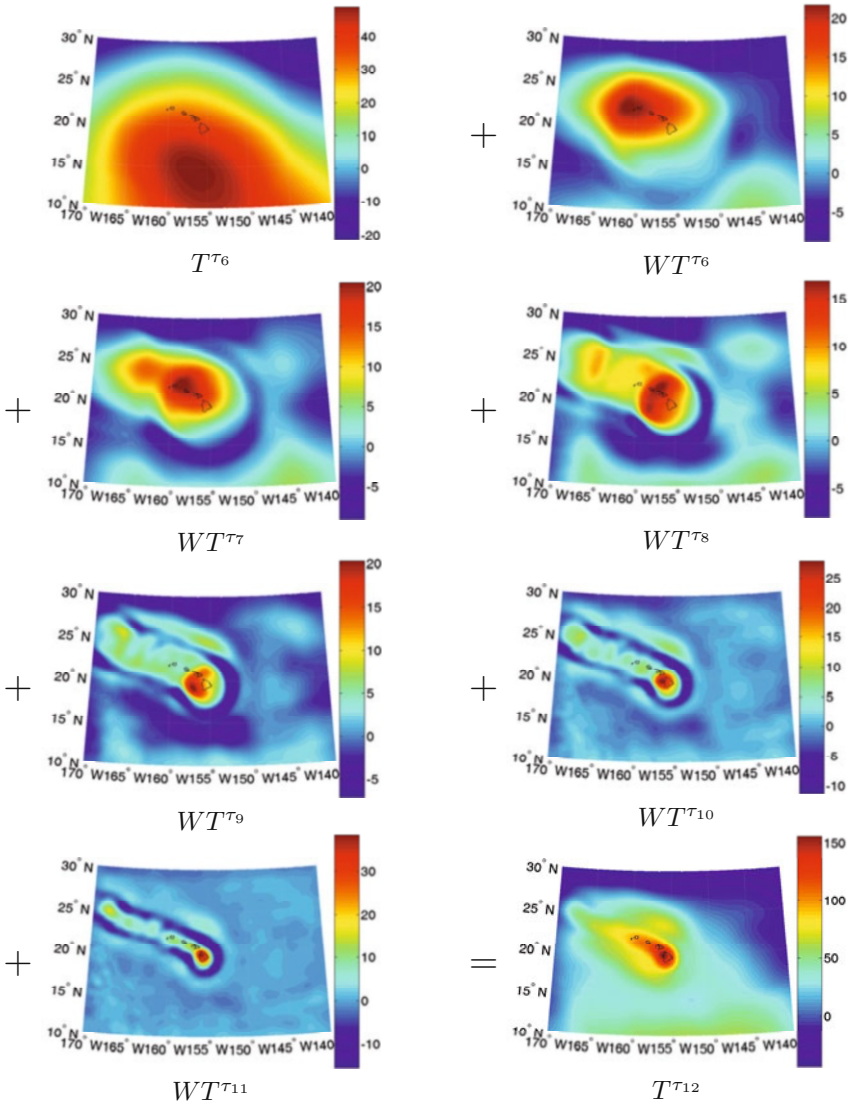

FIGURE 2.13. Multiscale reconstruction of the disturbing potential T in $[\mathrm{m}^2\mathrm{s}^{-2}]$ from vertical deflections Θ for the Hawaiian (plume) area using the scaling function g^{τ} (a rough low-pass filtering T^{τ_6} at scale $j = 6$ is improved by several band-pass filters WT^{τ_j} at scales $j = 6, \ldots, 11$, the last illustration shows the approximation $T^{\tau_{12}}$ of the disturbing potential T at scale $j = 12$, (from the Ph.D.-thesis [9], Geomathematics Group, University of Kaiserslautern).

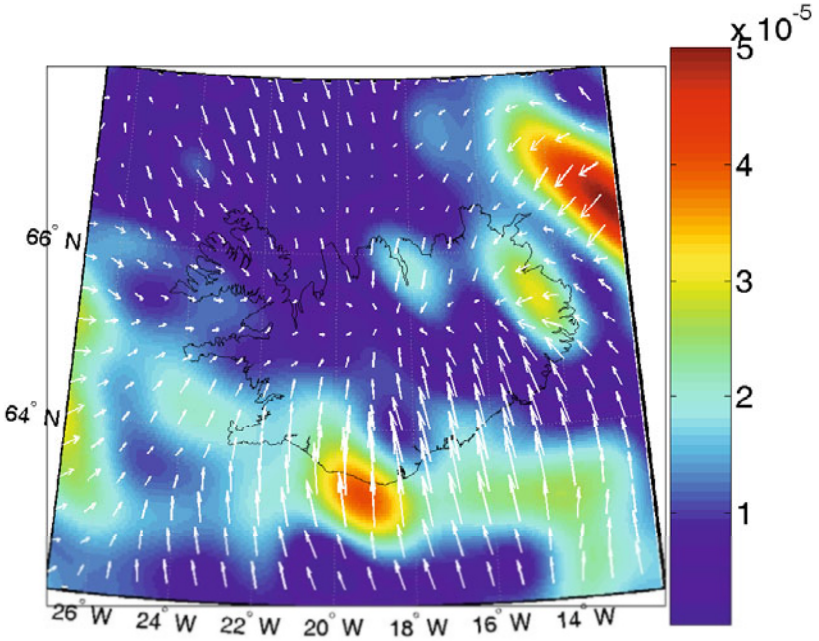

FIGURE 2.14. Illustration of the vertical deflections Θ in the region of Iceland (see [15]).

potential of the Earth is influenced by its topography, a look at a topographic map shows that the sector located more Eastern is (probably) caused by the Vatnajökull glacier (being the biggest glacier in Europe).

All in all, from our multiscale reconstruction, it can be derived that the deeper parts of the mantle plume are located in the northern part of Iceland (compare the lower scales in Figure 2.15) while shallower parts are located further south (compare the higher scales in Figure 2.15). As the North American plate moves westward and the Eurasian plate eastward, new crust is generated on both sides of the Mid-Atlantic Ridge. In the case of Iceland, which lies on the Mid-Atlantic Ridge, the neovolcanic zones are readily seen in Figure 2.16.

In Iceland, electrical production from geothermal power plants has been developed rapidly. Reflecting the geological situation, Iceland is a unique country with regard to utilization of geothermal energy, with more than 50% of its primary energy consumption coming from geothermal power plants. As shown in Figure 2.17, today's location of power plants in Iceland fits perfectly with the gravimetric investigations based on horizontal/vertical derivatives of the Earth's disturbing potential. As a matter of fact, only from these results it becomes obvious where future power plants should be placed for geothermal purposes.

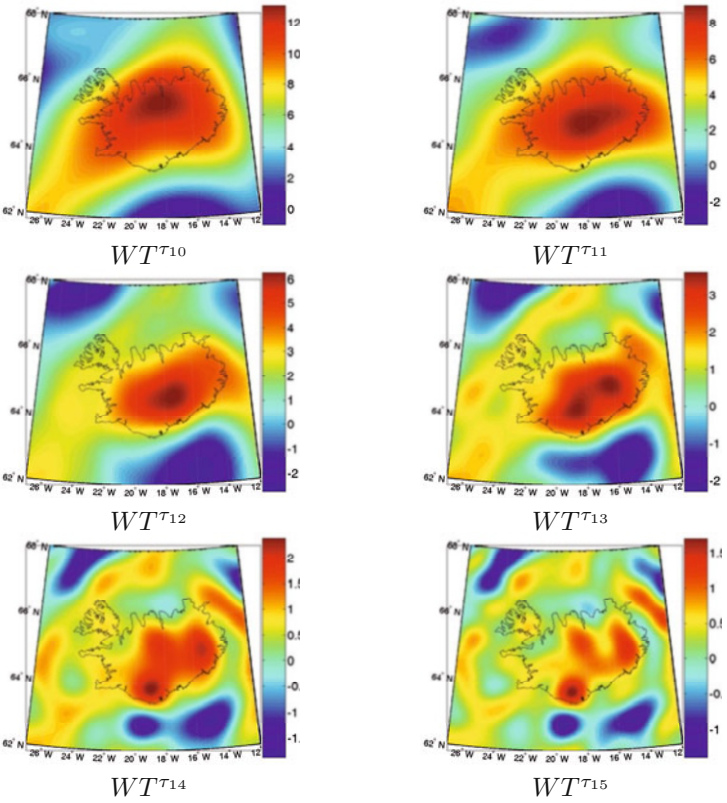

FIGURE 2.15. Band-pass filtered details WT^{τ_j} of the disturbing potential T in $[m^2 s^{-2}]$ from vertical deflections Θ in the region of Iceland with respect to the scales $j = 10, \ldots, 15$, (from [15]).

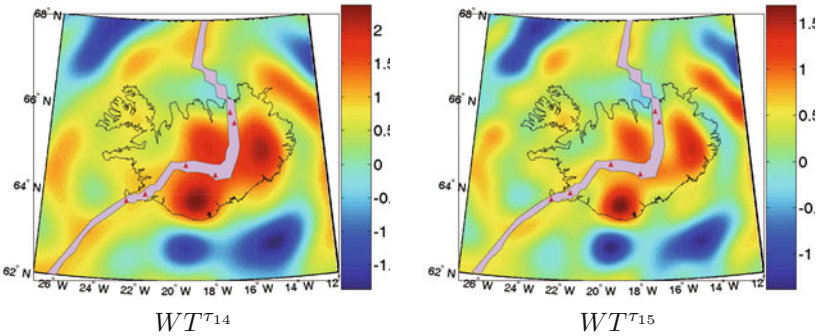

FIGURE 2.16. Band-pass filtered details WT^{τ_j} of the disturbing potential T in $\left[m^2 s^{-2}\right]$ from vertical deflections Θ in the region of Iceland for $j = 14, 15$ including the Mid-Atlantic Ridge (gray).

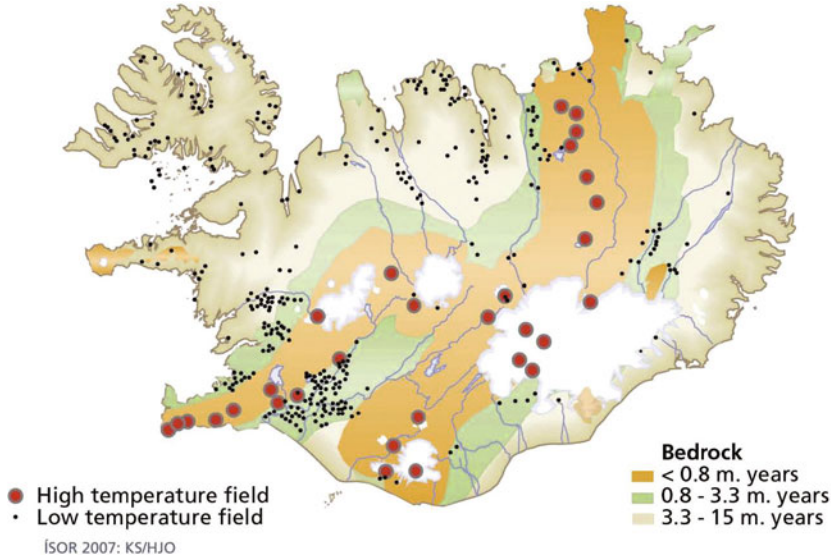

FIGURE 2.17. Geothermal power plants in Iceland [1, 37].

All in all, by the space-based multiscale techniques initiated by Freeden and Schreiner [21, 22] in gravitation we are able to come to interpretable results involving geological obligations in relation to hotspots/mantle plumes based on "surface interpretations" and just by looking at the anomalous behavior in terms of surface integrals without using the framework of Newton's volume integrals.

3. Interior gravitational potential and density distribution

3.1. Newton integral and Poisson equation

Seen from a mathematical point of view, the Earth's gravitational field v is a gradient field $v = \nabla V$, where the gravitational potential V is an infinitely often differentiable harmonic scalar field in the exterior of the Earth. As a consequence, the Earth's gravitational field v is an infinitely often differentiable vector field in the exterior of the Earth satisfying $\nabla \cdot v = 0,\ \nabla \wedge v = 0$.

According to the classical Newton Law of Gravitation (1687), knowing the density distribution of a region $\mathcal{G}$ such as the Earth, the gravitational potential (Newton potential) can be computed everywhere in $\mathbb{R}^3$. More explicitly, the gravitational potential V of the Earth's exterior $\mathcal{G}^c = \mathbb{R}^3 \backslash \overline{\mathcal{G}}$ is given by

$$V(x) = \gamma \int_{\mathcal{G}} F(y) G(\Delta; |x-y|)\, dV(y), \qquad x \in \mathbb{R}^3 \backslash \overline{\mathcal{G}}, \tag{3.1}$$

with the so-called fundamental solution $G(\Delta;\cdot)$ of the Laplace equation given by

$$G(\Delta;|x-y|) = -\frac{1}{4\pi}\frac{1}{|x-y|}, \tag{3.2}$$

and the gravitational constant γ, where F is the density function. Since γ is a constant, it has no effect on any of the following considerations. Hence, from now on, for the sake of simplicity, we neglect the gravitational constant γ in all equations, but it will be observed in numerical computations. The properties of the gravitational potential V in the Earth's exterior are easily described as follows:

(i) V is *harmonic* in $\mathbb{R}^3\backslash\overline{\mathcal{G}}$, i.e., $\Delta_x V(x) = 0,\ x \in \mathbb{R}^3\backslash\overline{\mathcal{G}}$.
(ii) V is *regular at infinity*, i.e., $|V(x)| = O\left(|x|^{-1}\right),\ |x| \to \infty$.

Let $\mathcal{G} \subset \mathbb{R}^3$ be a *regular region*, i.e., a bounded region $\mathcal{G} \subset \mathbb{R}^3$ dividing $\mathbb{R}^3$ uniquely into the inner space $\mathcal{G}$ and the outer space $\mathcal{G}^c = \mathbb{R}^3\backslash\overline{\mathcal{G}}$, $\overline{\mathcal{G}} = \mathcal{G} \cup \partial\mathcal{G}$, such that the boundary $\partial\mathcal{G}$ is an orientable smooth Lipschitzian manifold of dimension 2 (for example, ball, ellipsoid, geoid, Earth or appropriate cuboidal parts of it). It is already known, that the Newton (volume) integral over a regular region $\mathcal{G}$, corresponding to a mass density distribution F satisfies the Laplace equation in the outer space $\mathcal{G}^c = \mathbb{R}^3\backslash\overline{\mathcal{G}}$. Clearly, this property is an immediate consequence of the harmonicity of the fundamental solution for the Laplace equation (see, e.g., [40]).

Theorem 3.1. *Let $F : \overline{\mathcal{G}} \to \mathbb{R}$ be an integrable, bounded function. Then*

$$V(x) = \int_{\mathcal{G}} F(y)\ G(\Delta;|x-y|)\ dV(y), \qquad x \in \mathcal{G}^c, \tag{3.3}$$

satisfies

$$\Delta_x V(x) = \Delta_x \int_{\mathcal{G}} F(y)\ G(\Delta;|x-y|)\ dV(y) = 0, \quad x \in \mathcal{G}^c, \tag{3.4}$$

i.e., V is harmonic in $\mathcal{G}^c$.

Next, we are interested in showing that the Newton integral in the inner space satisfies the Poisson equation at least under some canonical conditions on the density function (see, e.g., [15]).

Theorem 3.2. *Let $F : \overline{\mathcal{G}} \to \mathbb{R}$ be of class $C^{(0)}(\overline{\mathcal{G}})$. Then V as defined by* (3.3) *is of class $C^{(1)}(\overline{\mathcal{G}})$. Furthermore, we have*

$$\nabla_x V(x) = \int_{\mathcal{G}} F(y)\ \nabla_x G(\Delta;|x-y|)\ dV(y), \qquad x \in \overline{\mathcal{G}}. \tag{3.5}$$

Proof. The fundamental solution

$$G(\Delta;|x-y|) = -\frac{1}{4\pi}\frac{1}{|x-y|}, \qquad |x-y| \neq 0, \tag{3.6}$$

admits a "regularization" (mollification) of the form

$$G_0^\tau(\Delta;|x-y|) = \begin{cases} -\dfrac{3\tau^2-|x-y|^2}{8\pi\tau^3}, & |x-y| \le \tau, \\ -\dfrac{1}{4\pi|x-y|}, & \tau < |x-y|. \end{cases} \tag{3.7}$$

For brevity, we set

$$V_0^\tau(x) = \int_{\mathcal{G}} F(y)\ G_0^\tau(\Delta;|x-y|)\ dV(y), \quad x \in \overline{\mathcal{G}}. \tag{3.8}$$

The integrands of V and V_0^τ only differ in the ball $\mathcal{B}_\tau(x)$ around the point x with radius τ. Moreover, the function $F : \overline{\mathcal{G}} \to \mathbb{R}$ is supposed to be continuous on $\overline{\mathcal{G}}$. Hence, it is uniformly bounded on $\overline{\mathcal{G}}$ and we derive

$$\begin{aligned} \sup_{x\in\overline{\mathcal{G}}} |V(x) - V_0^\tau(x)| &= \mathcal{O}\left(\int_{\mathcal{B}_\tau(x)} |G(\Delta;|x-y|) - G_0^\tau(\Delta;|x-y|)|\ dV(y) \right) \\ &= \mathcal{O}(\tau^2). \end{aligned} \tag{3.9}$$

Therefore, V is of class $\mathrm{C}^{(0)}(\overline{\mathcal{G}})$ as the limit of a uniformly convergent sequence of continuous functions on $\overline{\mathcal{G}}$. We let

$$v(x) = \int_{\mathcal{G}} F(y)\ \nabla_x G(\Delta;|x-y|)\ dV(y), \quad x \in \overline{\mathcal{G}}, \tag{3.10}$$

and

$$v_0^\tau(x) = \int_{\mathcal{G}} F(y)\ \nabla_x G_0^\tau(\Delta;|x-y|)\ dV(y), \quad x \in \overline{\mathcal{G}}. \tag{3.11}$$

As $|\nabla_x G(\Delta;|x-y|)| = \mathcal{O}(|x-y|^{-2})$, the integrals v and v_0^τ exist for all $x \in \overline{\mathcal{G}}$. It is not hard to see that

$$\sup_{x\in\overline{\mathcal{G}}} |v(x) - v_0^\tau(x)| = \sup_{x\in\overline{\mathcal{G}}} |v(x) - \nabla_x V_0^\tau(x)| = \mathcal{O}(\tau). \tag{3.12}$$

Consequently, v is a continuous vector field on $\overline{\mathcal{G}}$. Moreover, as the relation (3.12) holds uniformly on $\overline{\mathcal{G}}$, we obtain

$$v(x) = \nabla_x V(x) = \int_{\mathcal{G}} F(y)\ \nabla_x G(\Delta;|x-y|)\ dV(y). \tag{3.13}$$

This is the desired result. □

Remark 3.3. The proof is standard (see, e.g., [22]). Its explicit formulation, however, is helpful to understand the feature extraction method.

Next, we come to the Poisson equation under the assumption of Hölder continuity for the function F on $\overline{\mathcal{G}}$.

Theorem 3.4. *If F is of class $C^{(0,\mu)}(\overline{\mathcal{G}})$, $\mu \in (0,1]$, then the Poisson differential equation*

$$\Delta_x \int_{\mathcal{G}} F(y)\ G(\Delta; |x-y|)\ dV(y) = F(x) \tag{3.14}$$

holds true for all $x \in \mathcal{G}$.

The proof can be found in any textbook on potential theory, e.g., [15]. It is also part of Chapter 5 of this handbook.

The fundamental solution $G_0^\tau(\Delta;\cdot)$ as well as the (ordinary) *Haar function* given by

$$H_0^\tau(|x-y|) = \Delta_x G_0^\tau(\Delta; |x-y|) = \begin{cases} \frac{3}{4\pi\tau^3}, & |x-y| \le \tau, \\ 0, & |x-y| > \tau, \end{cases} \tag{3.15}$$

are depicted in Figure 3.1 for different values of τ.

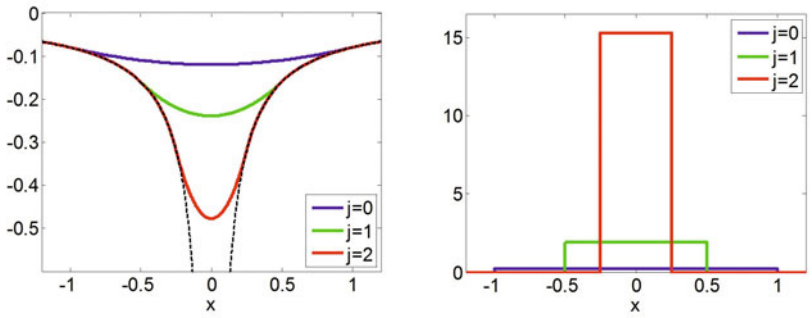

FIGURE 3.1. Sectional profile of the functions $G_0^\tau(\Delta;\cdot)$ (left) and H_0^τ (right) for the values $\tau = 2^{-j}, j = 0, 1, 2$. The black line in the left figure indicates the profile of the fundamental solution $G(\Delta;\cdot)$.

The critical point that will be expected in numerics of feature extraction by means of regularized potentials V_0^τ is the discontinuity of the Laplace derivative of $G_0^\tau(\Delta;\cdot)$, i.e., the (ordinary) Haar function H_0^τ. This is the reason why we are interested in higher-order Taylor expansions of the fundamental solution leading to a polynomial of degree $n+2$ given by $r \mapsto G_n^\tau(\Delta; r),\ r \in [0, \infty,)$ with

$$G_n^\tau(\Delta; r) = \begin{cases} -\frac{1}{4\pi r}, & \tau \le r, \\ \frac{1}{8\pi\tau^{n+3}} \sum_{l=0}^{n+1} \left((-1)^l (n+1) \binom{n+2}{l}\right) \tau^{n+2-l} r^l & \\ \quad + \frac{1}{8\pi\tau^{n+3}} \sum_{l=0}^{n+1} \left(2(-1)^{l+1} \binom{n+2}{l+1}\right) \tau^{n+2-l} r^l & \\ \quad + (-1)^{n+2}\ \frac{n+1}{8\pi\tau^{n+3}}\ r^{n+2}, & 0 \le r < \tau \end{cases} \tag{3.16}$$

instead of

$$G_0^\tau(\Delta;r) = \begin{cases} -\frac{1}{4\pi r}, & \tau \le r, \\ -\frac{3\tau^2 - r^2}{8\pi\tau^3}, & 0 \le r < \tau, \end{cases} \tag{3.17}$$

so that

$$H_n^\tau(r) = \Delta_x G_n^\tau(\Delta;r) = \begin{cases} 0, & \tau < r, \\ \frac{(n+1)(n+2)(n+3)}{8\pi} \frac{(\tau - r)^n}{\tau^{n+3}}, & 0 \le r \le \tau. \end{cases} \tag{3.18}$$

It is easy to see that $r \mapsto G_n^\tau(\Delta;r), r \in [0,\infty)$, is $(n+1)$-times continuously differentiable and $r \mapsto H_n^\tau(r), r \in [0,\infty)$, is $(n-1)$-times continuously differentiable (where, by convention in case of H_0^τ, (-1)-times continuously differentiable means piecewise continuous). Moreover, we notice that H_0^τ for $n = 0$ is the ordinary (spherically symmetric) τ-Haar function in $\mathbb{R}^3$.

As a consequence of our preparatory considerations we obtain the following statement that serves as strategic basis for our forthcoming approach to geological feature extraction.

Theorem 3.5. *For $n \in \mathbb{N}_0$, the "τ-potential functions" of order n*

$$V_n^\tau(x) = \int_{\mathcal{G}} G_n^\tau(\Delta; |x-y|) F(y)\, dV(y) \tag{3.19}$$

and the "τ-contrast functions" of order n

$$F_n^\tau(x) = \int_{\mathcal{G}} H_n^\tau(|x-y|) F(y)\, dV(y), \tag{3.20}$$

satisfy the limit relations

$$\lim_{\tau \to 0} |V(x) - V_n^\tau(x)| = 0, \quad x \in \mathcal{G} \tag{3.21}$$

and

$$\lim_{\tau \to 0} |F(x) - F_n^\tau(x)| = 0, \quad x \in \mathcal{G}, \tag{3.22}$$

provided that F is ($\mathrm{C}^{(0,\mu)}$-Hölder) continuous in the neighborhood of $x \in \mathcal{G}$.

The kernels $G_n^\tau(\Delta;\cdot)$ and H_n^τ are called *"τ-fundamental scaling function of order n"* and *"τ-Haar scaling function of order n"*, respectively. It should be remarked that $G_n^\tau(\Delta;\cdot)$ is constructed in such a way that the normalization condition

$$\int_{\mathbb{R}^3} \Delta_x G_n^\tau(\Delta;|x|)\, dV(x) = \int_{\mathbb{R}^3} H_n^\tau(|x|)\, dV(x) = 1 \tag{3.23}$$

holds true for all $\tau > 0$ and all $n \in \mathbb{N}_0$.

Unfortunately, τ-potential functions V_n^τ do not generally show a faster convergence to V than τ-potential functions V_0^τ; more concretely, we have

$$\begin{aligned}\sup_{x\in\overline{\mathcal{G}}}|V(x)-V_n^\tau(x)| &= \mathcal{O}\left(\int_{\mathcal{B}_\tau(x)}|G(\Delta;|x-y|)-G_n^\tau(\Delta;|x-y|)|\;dV(y)\right)\\ &= \mathcal{O}(\tau^2)\end{aligned} \tag{3.24}$$

for $n\in\mathbb{N}_0$. Finally it should be alluded that

$$\lim_{\tau\to 0}\sup_{x\in\overline{\mathcal{G}}}|\alpha(x)F(x)-F_n^\tau(x)|=0, \tag{3.25}$$

where $\alpha(x)$ is the solid angle subtended at $x\in\overline{\mathcal{G}}$ by the boundary surface $\partial\mathcal{G}$.

Remark 3.6. The solid angle $\alpha(x)$ in Equation (3.25) is necessary due to the fact that the support of $H_n^\tau(|\cdot-x|)$ is cut of at the boundary $\partial\mathcal{G}$ for all $\tau>0$ with $x\in\partial\mathcal{G}$.

3.2. Multiscale postprocessing of signature decorrelation

Next we deal with new mathematical mechanisms for a deeper interpretation and a better understanding of gravimetrically available pre-information inside a regular region $\mathcal{G}$. In order to make the decorrelation mechanisms transparent, our considerations start from the unrealistic assumption that the potential V is known everywhere in $\overline{\mathcal{G}}$. Our purpose is to demonstrate how the multiscale procedure for the potential canonically transfers to the density by use of "Poisson derivatives". All in all, the context of this section is meant as conceptual preparation of the Haar-type inversion process (see also [3]) discussed later on.

Suppose that $\{\tau_j\}_{j\in\mathbb{N}_0}$ is a positive, monotonously decreasing sequence with $\lim_{j\to\infty}\tau_j=0$. For $j\in\mathbb{N}_0$, we consider the differences

$$\Psi_{G_n^{\tau_j}}(\Delta;|x-y|)=G_n^{\tau_{j+1}}(\Delta;|x-y|)-G_n^{\tau_j}(\Delta;|x-y|) \tag{3.26}$$

and

$$\Psi_{H_n^{\tau_j}}(|x-y|)=H_n^{\tau_{j+1}}(|x-y|)-H_n^{\tau_j}(|x-y|). \tag{3.27}$$

$\Psi_{G_n^{\tau_j}}(\Delta;\cdot)$ and $\Psi_{H_n^{\tau_j}}$ are called *"τ_j-fundamental wavelet function of order n"* and *"τ_j-Haar wavelet function of order n"*, respectively (see Figure 3.2).

The associated *"τ_j-potential wavelet functions" of order n* and the *"τ_j-contrast wavelet functions" of order n* are given by

$$(WV)_n^{\tau_j}(x)=\int_{\mathcal{G}}\Psi_{G_n^{\tau_j}}(\Delta;|x-y|)F(y)\;dV(y) \tag{3.28}$$

and

$$(WF)_n^{\tau_j}(x)=\int_{\mathcal{G}}\Psi_{H_n^{\tau_j}}(|x-y|)F(y)\;dV(y). \tag{3.29}$$

The τ_j-potential wavelet functions of order n and the τ_j-contrast wavelet functions of order n, respectively, characterize the successive *detail information* contained in $V_n^{\tau_{j+1}}-V_n^{\tau_j}$ and $F_n^{\tau_{j+1}}-F_n^{\tau_j}$, $j\in\mathbb{N}_0$. In other words, we are able to recover the

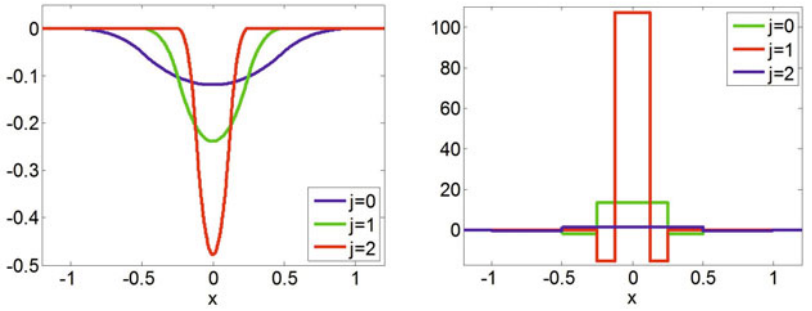

FIGURE 3.2. Sectional profile of the wavelet functions $\Psi_{G_n^{\tau_j}}(\Delta;\cdot)$ (left) and $\Psi_{H_n^{\tau_j}}(\cdot)$ (right) for $n=0$ and $\tau_j = 2^{-j}, j = 0,1,2$.

potential V and the contrast function, i.e., the "density signature" F, respectively, in form of "band structures"

$$(WV)_n^{\tau_j} = V_n^{\tau_{j+1}} - V_n^{\tau_j}, \tag{3.30}$$

and

$$(WF)_n^{\tau_j} = F_n^{\tau_{j+1}} - F_n^{\tau_j}. \tag{3.31}$$

As a consequence, the essential problem to be solved in multiscale extraction of geological features is to identify those detail information, i.e., band structures in (3.30), which contain specific geological (density) characteristics in (3.31), for example, aquifers, salt domes, etc.

Seen from a numerical point of view, it is remarkable that both wavelet functions $y \mapsto \Psi_{G_n^{\tau_j}}(\Delta;|x-y|)$ and $y \mapsto \Psi_{H_n^{\tau_j}}(|x-y|)$ vanish outside a ball around the center x due to their construction, i.e., these functions are spacelimited showing a ball as local support. Furthermore, the support becomes smaller and smaller with increasing scale parameter j, so that more and more high frequency phenomena can be highlighted without changing the features outside the balls. Explicitly written out in our nomenclature we obtain for $x \in \overline{\mathcal{G}}$

$$(WV)_n^{\tau_j}(x) = \int_{\mathcal{B}_{\tau_j}(x)\cap\mathcal{G}} \Psi_{G_n^{\tau_j}}(\Delta;|x-y|)F(y)\,dV(y), \tag{3.32}$$

and

$$(WF)_n^{\tau_j}(x) = \int_{\mathcal{B}_{\tau_j}(x)\cap\mathcal{G}} \Psi_{H_n^{\tau_j}}(|x-y|)F(y)\,dV(y). \tag{3.33}$$

Forming the sums

$$\sum_{j=0}^{J-1}(WV)_n^{\tau_j}(x) = \sum_{j=0}^{J-1}\left(V_n^{\tau_{j+1}}(x) - V_n^{\tau_j}(x)\right), \tag{3.34}$$

and

$$\sum_{j=0}^{J-1}(WF)_n^{\tau_j}(x) = \sum_{j=0}^{J-1}\left(F_n^{\tau_{j+1}}(x) - F_n^{\tau_j}(x)\right), \tag{3.35}$$

we are easily led to

$$V_n^{\tau_J}(x) = V_n^{\tau_0}(x) + \sum_{j=0}^{J-1}(WV)_n^{\tau_j}(x) \tag{3.36}$$

and

$$F_n^{\tau_J}(x) = F_n^{\tau_0}(x) + \sum_{j=0}^{J-1}(WF)_n^{\tau_j}(x). \tag{3.37}$$

Thus, we finally end up with the following multiscale relations

$$V(x) = \lim_{J\to\infty} V_n^{\tau_J}(x) = V_n^{\tau_0}(x) + \sum_{j=0}^{\infty}(WV)_n^{\tau_j}(x) \tag{3.38}$$

and

$$\alpha(x)F(x) = \lim_{J\to\infty} F_n^{\tau_J}(x) = F_n^{\tau_0}(x) + \sum_{j=0}^{\infty}(WF)_n^{\tau_j}(x) = \lim_{J\to\infty}\Delta_x V_n^{\tau_J}(x), \tag{3.39}$$

i.e.,

$$\alpha(x)F(x) = \Delta_x V_n^{\tau_0}(x) + \sum_{j=0}^{\infty}\Delta_x(WV)_n^{\tau_j}(x). \tag{3.40}$$

Altogether, the potential V as well as the contrast function, i.e., the "density signature" F can be expressed in additive way as a low-pass filtered signal $V_n^{\tau_0}$ and $F_n^{\tau_0}$ and successive band-pass filtered signals $(WV)_n^{\tau_j}$ and $(WF)_n^{\tau_j}$, $j = 0, 1, \ldots$, respectively.

It should be mentioned that our multiscale approach is constructed such that, within the spectrum of all wavebands (cf. (3.30), (3.31)), certain rock formations or aquifers, respectively, may be associated to a specific waveband characterizing typical features within the multiscale reconstruction (see Figure 3.3). Each scale parameter in the decorrelation is assigned to a data function which corresponds to the associated waveband and, thus, leads to a low-pass approximation of the data at a particular resolution.

Finally it should be noted that the key ideas of multiscale approximation as presented here lead back to evaluation methods proposed by Freeden and Schreiner [21], Freeden and Blick [13], and particularly Freeden and Gerhards [15]. For the sake of simplicity, the adaptation of this approach to the requirements of gravitational potential as well as density distribution is explained only in scale discrete form, a scale continuous formulation as presented in [21] is canonical. A variety of numerical tests and case studies of our approach are found in the Ph.D.-theses [2, 49].

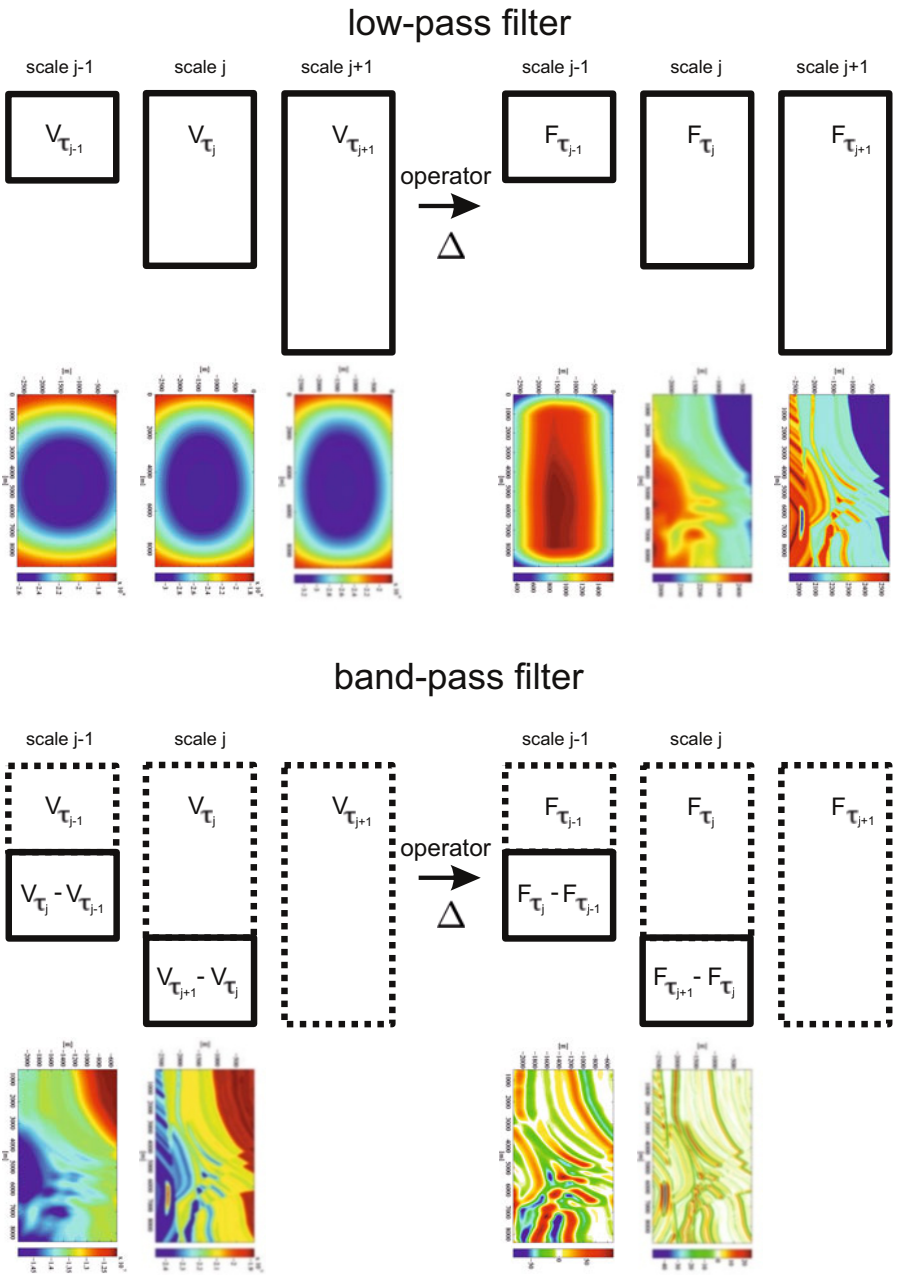

FIGURE 3.3. Schematic visualization of the multiscale decorrelation mechanism (see [3]).

3.3. Decorrelation of the Marmousi test model

Next we deal with the decorrelation of the geological signatures of a test area, namely the well-known Marmousi potential and density model (we use the canonically constructed 3D-version of the Marmousi model as proposed in the Ph.D.-thesis [2], see Figures 3.4, 3.5). In accordance with this standard test model (see also [42, 67]), the contrast function F is available as a fully interpreted 3D Marmousi density model extension (see Figure 3.6).

In order to validate the decorrelation abilities of our multiscale approach presented in the last section, we first perform a decomposition of the potential based on Eq. (3.38) (see Figure 3.7). Obviously, the low-pass filtered data, i.e., the τ_j-potential functions $V_n^{\tau_j}$ (see Eq. (3.19)) provide no essential structural information (see Figure 3.7, left column). However, for smaller scale values τ_j, by going over to finer detail information involving τ_j-wavelet potential functions, we already notice essential trends of the geological situation of the original density model (see Figure 3.7, right column).

Keeping the properties of the Newton volume integral in mind, we are not very surprised that, following the construction principles as proposed in our multiscale approach, the decomposition of the 3D Marmousi density model F based on Eq. (3.39) (Figure 3.8, left), in fact, shows a significant correlation to the decomposition of the τ_j-wavelet potential functions. Nevertheless, the τ_j-wavelet contrast functions (Figure 3.8, right) yield additional information, for example, the separation of all density transitions can be clearly detected at scale $j = 9$. This observation is of great significance in geothermal research, where the fracture transitions play a particular role for detecting areas of internal water flow.

Next we modify the original potential function V by adding three perturbations in form of mass points, i.e., fundamental solutions, at different locations obtaining the potential V_{mod}. Our purpose is to determine the locations of these three disturbances for the depth detection of geological formations. It should be noted that a decorrelation of the data with low-frequency wavelets (i.e., low values j) basically means focusing the multiscale approach on low-frequency signal components. Wavelets to higher values j allow to focus on the high-frequency interference.

As a consequence, our multiscale decorrelation mechanism shows that the low-pass filtered signals of V and V_{mod} are structurally identical (see Figures 3.7 and 3.9). However, at scale $j = 9$ (see Figure 3.10), we can identify the exact location of the centers of the introduced fundamental solutions (i.e., buried mass points) in the band-pass filtered data.

3.4. Gravimetry and Haar-type inversion

The inversion of Newton's Law of Gravitation (3.1), i.e., the determination of the internal "density function" from information of the gravitational potential is known as the *gravimetry problem*: To be more concrete, the gravimetry problem amounts to the problem of determining the "density function" F from (discrete) information of the gravitational potential V in $\mathbb{R}^3$ in accordance with the integral

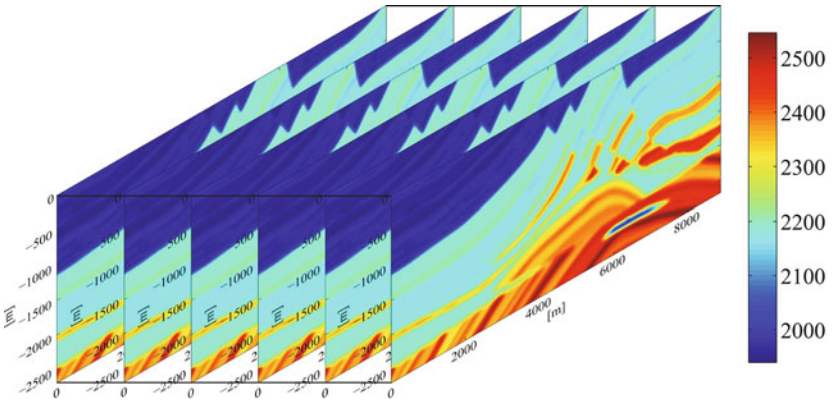

FIGURE 3.4. Artificially constructed 3D Marmousi density model.

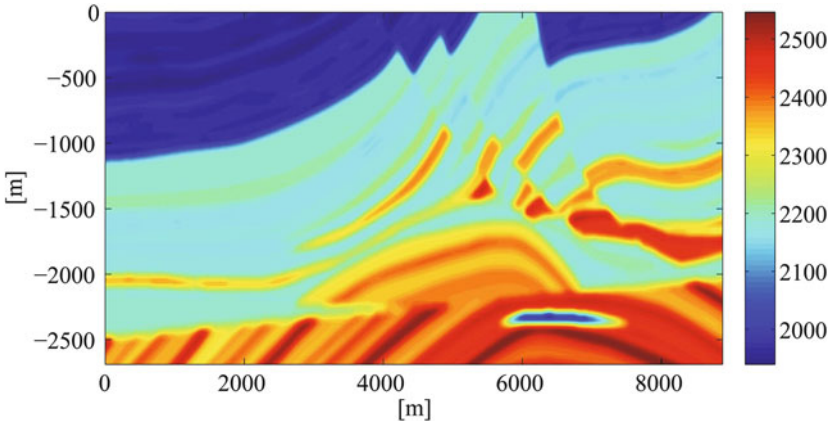

FIGURE 3.5. Cross-section of the 3D Marmousi density model (cf. [67]).

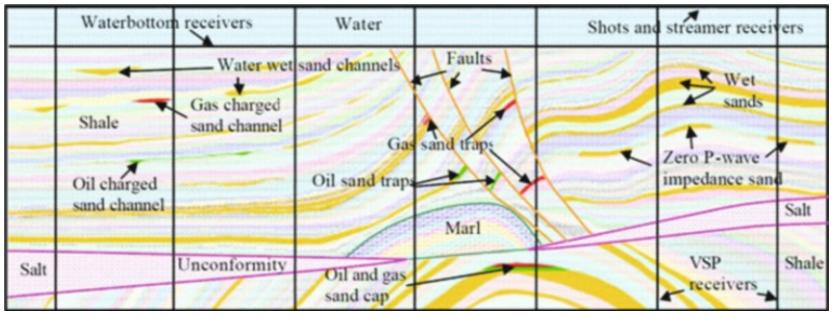

FIGURE 3.6. Marmousi density model and its geological interpretation (cf. [42]).

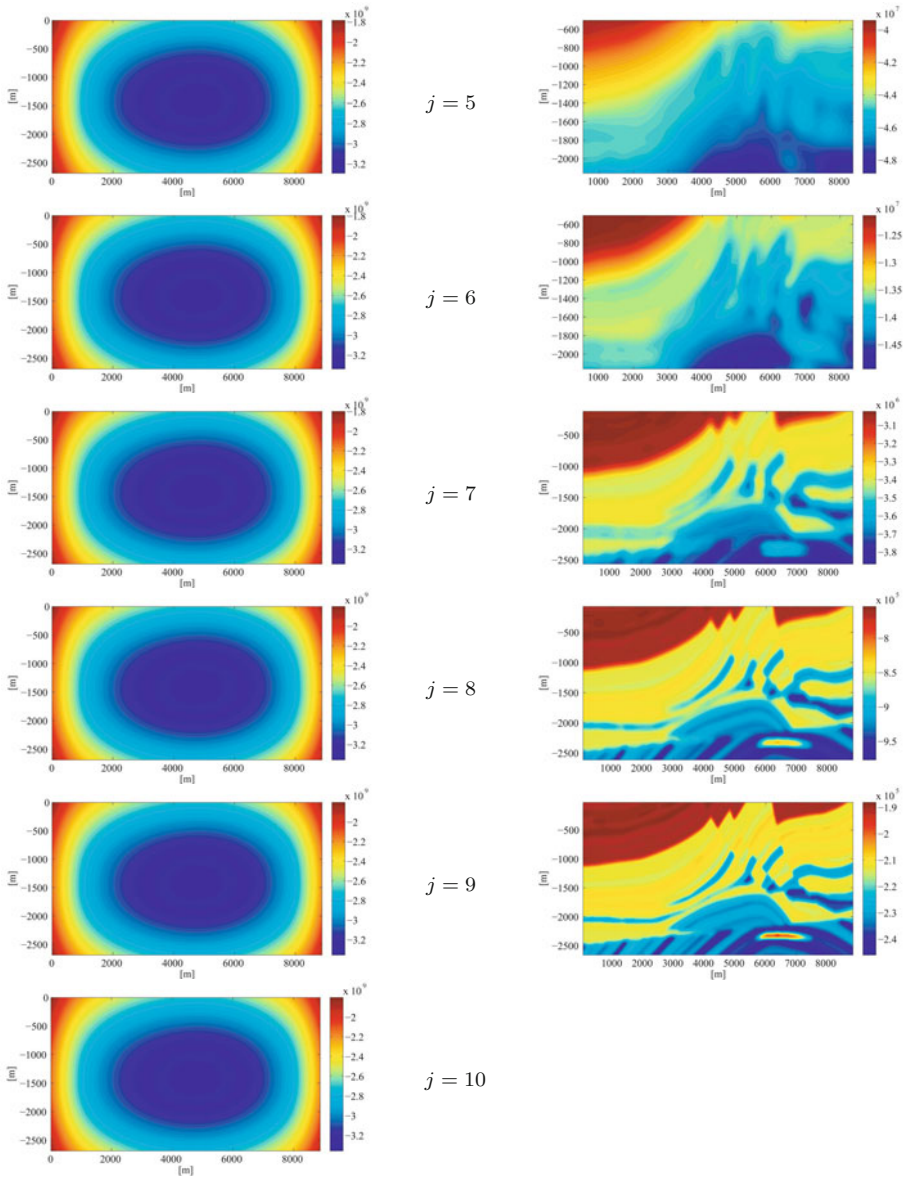

FIGURE 3.7. Decomposition of the 3D Marmousi potential in low-pass ($V_n^{\tau_j}$, left) and band-pass filtered parts ($(WV)_n^{\tau_j}$, right) for the sequence $\tau_j = 9200m \cdot 2^{-j}$ and $n = 0$ in $[kg/m]$. The choice of the sequence is adapted to the length of the density model (from the Ph.D.-thesis [2], Geomathematics Group, University of Kaiserslautern).

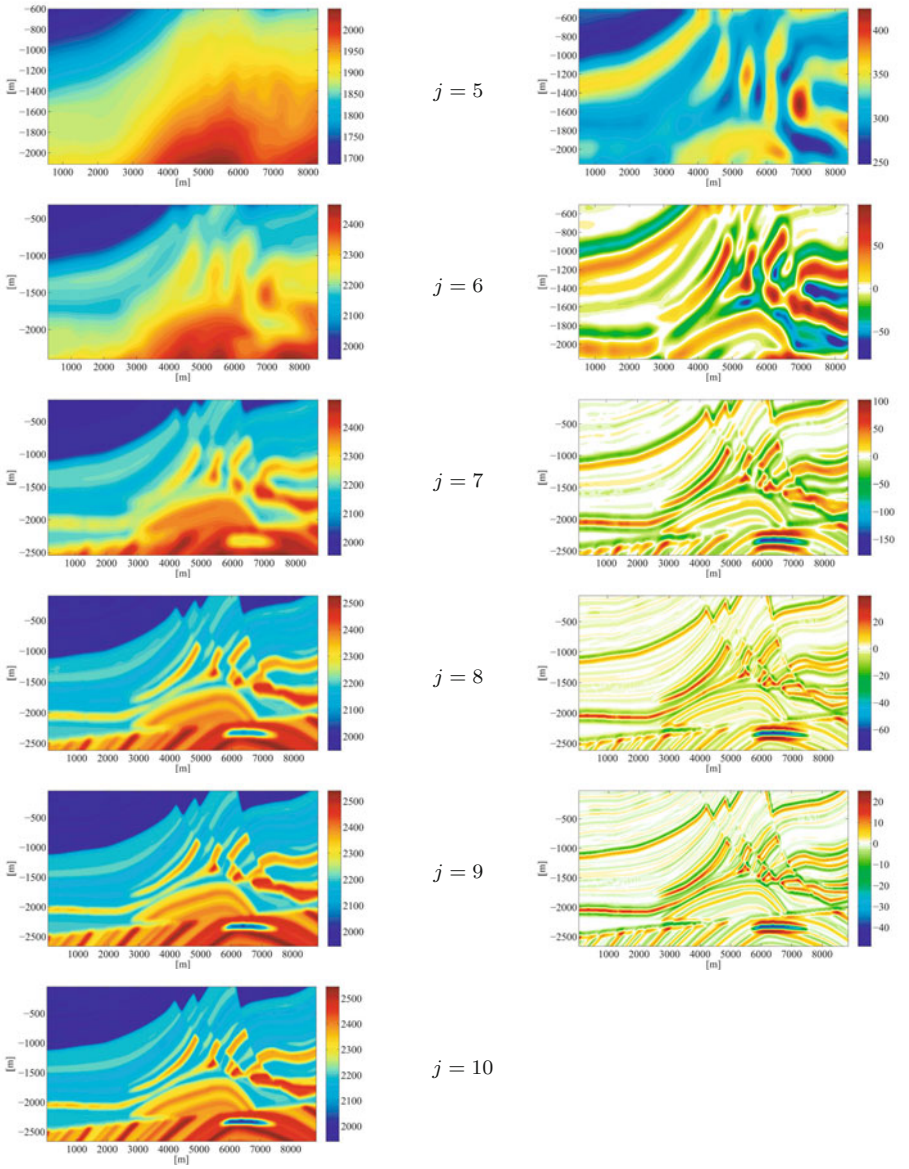

FIGURE 3.8. Decomposition of the 3D Marmousi density model into low-pass ($F_n^{\tau_j}$, left) and band-pass filtered parts ($(WF)_n^{\tau_j}$, right) for the sequence $\tau_j = 9200m \cdot 2^{-j}$ in $\left[kg/m^3\right]$ and $n = 0$. The choice of the sequence is adapted to the length of the density model (from the Ph.D.-thesis [2], Geomathematics Group, University of Kaiserslautern).

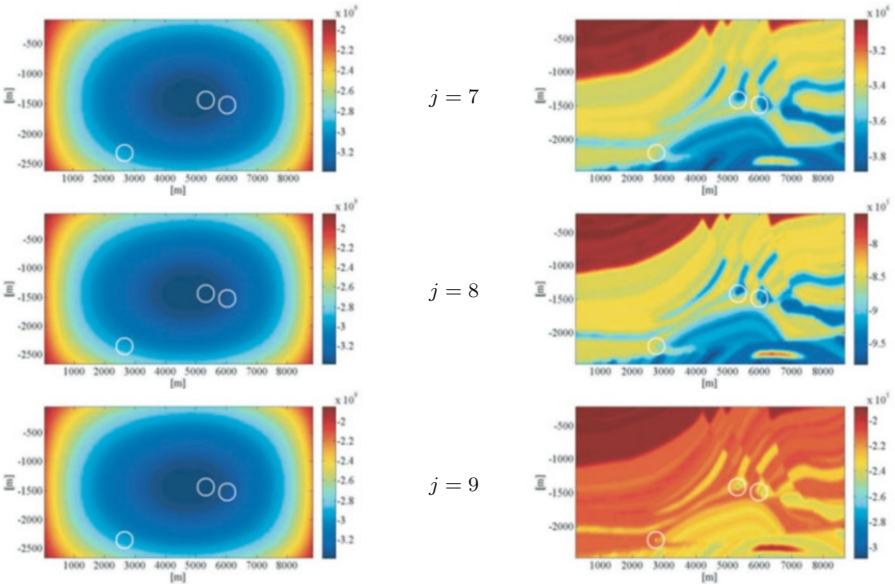

FIGURE 3.9. Decomposition of the modified 3D Marmousi potential V_{mod} in low-pass ($(V_{\text{mod}})_n^{\tau_j}$, left) and band-pass filtered parts ($(WV_{\text{mod}})_n^{\tau_j}$, right) for the sequence $\tau_j = 9200m \cdot 2^{-j}$ and $n = 0$ in $\left[\frac{kg}{m}\right]$. The choice of the sequence is adapted to the length of the density model.

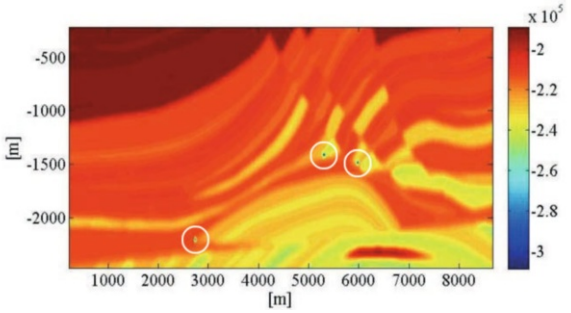

FIGURE 3.10. Illustration of the band-pass filtered signal $(WV_{\text{mod}})_n^{\tau_9}$ at scale $j = 9$ showing the locations of the three disturbing mass points, i.e., fundamental solutions and, consequently, the depth of the geological formations.

equation

$$V(x) = I[F](x) = \int_{\mathcal{G}} G(\Delta; |x-y|)F(y)\, dV(y), \quad x \in \mathbb{R}^3 \tag{3.41}$$

(note that we omit the gravitational constant γ).

In accordance with the mathematical *classification due to Hadamard*, the (classical) gravimetry problem of determining F from potential data on $\partial\mathcal{G}$, i.e., terrestrial gravitational data, violates all criteria, viz. existence, uniqueness and stability:

(i) (*Existence*) The potential V is harmonic outside $\mathcal{G}$. In accordance with the so-called Picard condition (see, e.g., [70]), a solution only exists if V belongs to (an appropriate subset in) the space of harmonic functions. However, it should be pointed out that this observation does not cause a numerical problem since, in practice, the information of V is only finite-dimensional. In particular, an approximation by an appropriate harmonic function is a natural ingredient of any practical method.

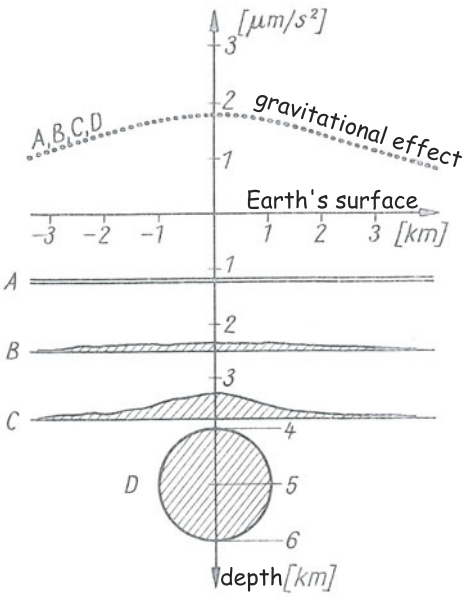

FIGURE 3.11. Equivalent gravity effect of different "sources" to generate the same gravitational potential on the Earth's surface (with kind permission of Teubner-publishing taken from [38] in modified form).

(ii) (*Uniqueness*) The most serious problem is the non-uniqueness of the solution (cf. Figure 3.11): The associated Fredholm integral operator I is of the first kind and has a kernel (null space) which is known (cf. [15, 20]) to coincide with the $L^2(\mathcal{G})$-orthogonal space of the closed linear subspace of all harmonic

functions on $\mathcal{G}$. Unfortunately, this orthogonal complement, i.e., the class of so-called anharmonic functions, is infinite-dimensional.

(iii) (*Stability*) Restricting the operator to harmonic densities leads to an injective mapping which has a discontinuous inverse implying an unstable solution.

Concerning the historical background, the question of the non-uniqueness for the classical gravimetry problem has been discussed extensively in literature, starting with a paper by Stokes [66] (for more details see, e.g., [15, 46, 47]). This calamity can be bypassed by imposing some reasonable additional condition on the density. A questionable condition, suggested by the mathematical structure of the Newton potential operator I, is to require that the density is harmonic. The approximate calculation of the harmonic density has already been implemented in several papers, whereas the problem of determining the anharmonic part seems to be still a great challenge. Due to the lack of an appropriate physical interpretation of the harmonic part of the density, various alternative variants have been discussed in the literature. In general, gravitational data yield significant information only about the uppermost part of the Earth's interior, which is not laterally homogeneous.

Seen from a mathematical point of view in constructive approximation, locally supported functions are not new, having been discussed already by Haar (1910). The importance of spacelimited (or in mathematical jargon locally supported) Haar kernels in view of a multiscale procedure is the "birth" to an entire "basis family" (scaling functions) by means of two operations, viz. dilations and translations.

In what follows, we recapitulate the already discussed "Haar philosophy" to realize an approximate determination of the mass density distribution inside $\mathcal{G}$ from discrete gravitational information. The essential tool is the regularization procedure of the Newton potential enabling to replace the integral equation (3.41) by the Fredholm integral equation of first kind

$$V_n^\tau(x) = \int_{\mathcal{G}} G_n^\tau(\Delta; |x-y|) F(y)\, dV(y), \quad x \in \mathbb{R}^3, \tag{3.42}$$

for a sufficiently large scale number J, so that the serious problem of non-uniqueness caused by the occurrence of anharmonic functions is not existent anymore for terrestrial potential data, however, at the price of non-harmonicity of the "regularizer" $y \mapsto G_n^{\tau_J}(\Delta; |x-y|)$ in a neighborhood outside $x \in \partial\mathcal{G}$.

In choosing a sufficiently large J we are aware of the fact (cf. Theorem 3.4) that

$$V(x) \simeq V_n^{\tau_J}(x) = \int_{\mathcal{G}} G_n^{\tau_J}(\Delta; |x-y|) F(y)\, dV(y), \quad x \in \mathbb{R}^3, \tag{3.43}$$

i.e., $V_n^{\tau_J}$ provides an approximation of the Newton integral (3.3) with negligible error. We remember

$$\Delta_x\, G_n^{\tau_J}(\Delta; |x-z|) = H_n^{\tau_J}(|x-z|) \tag{3.44}$$

for all $x, z \in \mathbb{R}^3$. From (3.44) it therefore follows that

$$\Delta_x \int_{\mathcal{G}} G_n^{\tau_J}(\Delta; |x-z|) F(z)\, dV(z) = F_n^{\tau_J}(x) \simeq \quad F(x), \quad x \in \mathcal{G}. \tag{3.45}$$

In order to realize a fully discrete approximation of F, we have to apply approximate integration formulas over $\mathcal{B}_{\tau_J}(x) \cap \overline{\mathcal{G}}$ leading to

$$V(x) \simeq V_n^{\tau_J}(x) \simeq \sum_{i=1}^{N_J} G_n^{\tau_J}(\Delta; |x - y_i^{N_J}|)\, w_i^{N_J} F(y_i^{N_J}), \tag{3.46}$$

where $w_i^{N_J}$, $y_i^{N_J} \in \mathcal{B}_{\tau_J}(x) \cap \overline{\mathcal{G}}$, $i = 1, \ldots, N_J$, are known weights and knots, respectively.

For the determination of the mass density we are confronted with the situation that all coefficients $a_i^{N_J} = w_i^{N_J} F(y_i^{N_J})$, $i = 1, \ldots, N_J$, are unknown. This, however, means that we have to solve a linear system, namely

$$V(x_k^{M_J}) = \sum_{i=1}^{N_J} G_n^{\tau_J}(\Delta; |x_k^{M_J} - y_i^{N_J}|) a_i^{N_J}, \quad k = 1, \ldots, M_J, \tag{3.47}$$

in order to determine the coefficients $a_i^{N_J}, i = 1, \ldots, N_J$, from *known gravitational values* $V(x_k^{M_J})$ at knots $x_k^{M_J} \in \mathbb{R}^3$, $k = 1, \ldots, M_J$.

Once all density values $F(y_i^{N_J})$, $i = 1, \ldots, N_J$, are available (note that the integration weights $w_i^{N_J}, i = 1, \ldots, N_J$, are known from the approximate integration rule), the density distribution F can be obtained from the formula

$$F(x) \simeq F_n^{\tau_J}(x) = \sum_{i=1}^{N_J} H_n^{\tau_J}(|x - y_i^{N_J}|)\, w_i^{N_J} F(y_i^{N_J}), \quad x \in \mathcal{G}. \tag{3.48}$$

Even more, fully discrete Haar filtered versions of F at lower scales, i.e., feature extraction, can be derived in accordance with the approximate integration rules

$$F_n^{\tau_j}(x) = \int_{\mathcal{G}} H_n^{\tau_j}(|x-y|) F(y)\, dV(y) \simeq \sum_{i=1}^{N_j} H_n^{\tau_j}(|x - y_i^{N_j}|) w_i^{N_j} F(y_i^{N_j}) \tag{3.49}$$

for $j = J_0, \ldots, J$, where $w_i^{N_j}$, $y_i^{N_j}$, $i = 1, \ldots, N_j$, are known weights and knots, respectively, such that we can take adventage of the fact that $\{y_1^{N_j}, \ldots, y_{N_j}^{N_j}\} \subset \{y_1^{N_J}, \ldots, y_{N_J}^{N_J}\} \subset \overline{\mathcal{G}}$, i.e., the sequence of knots $\{y_1^{N_j}, \ldots, y_{N_j}^{N_j}\} \subset \overline{\mathcal{G}}$ shows a hierarchical positioning.

Altogether, our approach yields Haar filtered versions (3.49) establishing a fully discrete (space-based) multiscale decomposition $F_n^{\tau_J}, \ldots, F_n^{\tau_{J_0}}$ of the density distribution F, such that an entire set of approximations is available from a single locally supported "mother function", i.e., the Haar kernel function, and this set provides useful "building block functions", which enable suitable storage and fast decorrelation of density data in consistency with geological formations.

It should be remarked that by discretizing the convolution integral by approximate integration in form of a suitable cubature formula, we arrive at a system of linear equations, which is sparse, since the utilized wavelet has a local support. The local support enables us to limit the multiscale technique to a local region, e.g., only to a relevant borehole area of interest, and guarantees that there is no change in the signature outside the support of the wavelets. All in all, our approach is given in such a way that the inversion of the equation system turns out to be numerically efficient and economical.

Remark 3.7. The linear systems occurring in this section can be handled by, e.g., use of domain decomposition techniques (see, e.g., [17, 19, 28–30, 34] and the references therein).

Remark 3.8. For simplicity, the input data of this subsection are potential data. In the same way, a linear system can be established by taking, e.g., free air gravity anomalies on the Earth's surface. In this case, however, we need Haar functions (3.18) of positive degrees n, since free air gravity anomalies are generated by a first-order derivative applied to the disturbing potential.

3.5. Improvement of in-borehole density signatures

Since both the actual potential V and the actual contrast function F, in general, cannot be measured directly inside the boundary surface $\partial\mathcal{G}$ and outside a neighborhood around the already existing boreholes without additional drilling, the a priori available potential and density information differ from the actual values and thus form only an approximation to the reality. If one associates a certain scale value τ_j within the multiscale process to the available potential data, we are given

$$V_n^{\tau_j}(x) = \int_{\mathcal{G}} G_n^{\tau_j}(\Delta; |x-y|)F(y)\ dV(y). \tag{3.50}$$

Often, in practice during borehole drilling, additional data are gathered by in-hole gravimetric measurements, so that we may assign a scale value τ_{j+1} to the improved potential data. If we now take the difference, we arrive at

$$V_n^{\tau_{j+1}}(x) - V_n^{\tau_j}(x) = \sum_{i=1}^{N_j} \Psi_{G_n^{\tau_j}}\left(\Delta; \left|x - y_i^{N_j}\right|\right) w_i^{N_j} F\left(y_i^{N_j}\right), \tag{3.51}$$

and

$$F_n^{\tau_{j+1}}(x) - F_n^{\tau_j}(x) = \sum_{i=1}^{N_j} \Psi_{H_n^{\tau_j}}\left(\left|x - y_i^{N_j}\right|\right) w_i^{N_j} F\left(y_i^{N_j}\right), \tag{3.52}$$

respectively. Once again, it should be emphasized that the linear system (3.51) can be evaluated efficiently and economically (note that the kernels $H_n^{\tau_j}$ as well as $\Psi_{G_n^{\tau_j}}$ and $\Psi_{H_n^{\tau_j}}$ have local support due to their construction and, hence, the systems of Equations (3.51) and (3.52) are sparse).

The improvement by additional data observation is shown using the example of the equation system (3.52). The input data for the inversion process are generated by smoothing of a cutout of the 3D Marmousi density model (see Figure 3.12, left for $F_n^{\tau_{j+1}}$). As a result of the inversion (see Figure 3.12, right), we obtain a sharper density model provided that the wavelet used in the inversion is sufficiently smooth, i.e., $n \geq 2$.

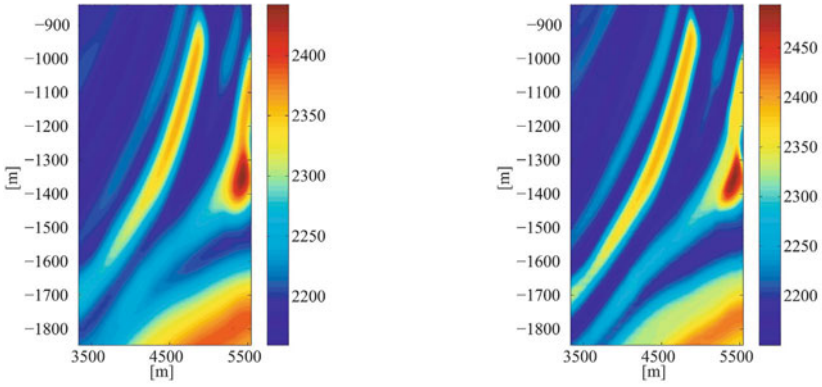

FIGURE 3.12. Illustration of the "best" data before the inversion $F_n^{\tau_{j+1}}$ (left) and the inversion result (right) for $n = 3$ and $j = 5$. The colors show the densities in [kg/m^3] (from the Ph.D.-thesis [2]).

An extensive parameter study in the Ph.D.-thesis [2] demonstrates that the inversion is numerically stable and efficient for smooth Haar-type kernels. Since the resulting relative error in the inversion depends continuously on the scale, there exists a reference interval, such that for each scale value inside this reference interval, an improvement of the data is achieved. This allows a certain tolerance in the choice of parameters.

Conclusions

Local knowledge of the gravity potential and its equipotential (level) surfaces giving information about mass distribution have become an important issue for exploration and prospecting. Indeed, the gravity field is a key component of future investigation. Seen from a numerical point of view, however, the way forward has to focus on two challenges:

(i) In reality, the distribution of geopotential data is far from being homogeneous with large gaps even in all European areas. In addition, the quality of the geopotential data under consideration is very distinct. A terrestrial data coverage now and in the foreseeable future is far from being satisfactory. For data supplementation and numerical stabilization, airborne and/or

spaceborne data are indispensable. This unfortunate situation causes particular mathematical attention for homogenization and unification to suppress undesired oscillation phenomena within the modeling process of the data.

(ii) Nowadays, the knowledge of geopotentials such as the Earth's gravitational potential and their anomalies have become an important and cost-effective issue in exploration technologies. However, it is commonly known that highly accurate sensors, when operating in an isolated manner, have their shortcomings. Combining globally available satellite data with regional airborne and/or local terrestrial observations within a physically founded and mathematically consistent multiscale process is therefore an essential step forward. In this respect, a "zooming-in" detection of specific geophysical attributes is an outstanding field of interest for validating the multiresolution method based on heterogeneous datasets and geophysically oriented multiscale "downward continuation" modeling of the different data sources starting from spaceborne data as trend solution via more accurate airborne data down to high-precision local data sets.

Geophysically relevant signatures are usually decomposed into single frequencies. Geomathematically, these techniques are well suited to resolve low and medium frequency phenomena, while their application to obtain high resolution models (such as descriptions of local orebodies, salt deposits, aquifers, etc.) is critical. Due to the quality of the data, i.e., the intrinsic scale amount of significant wave packages within the signal, spaceborne (i.e., satellite) data – continued downward to the Earth's surface – are the canonical point of departure for multiscale approximations of lower scale frequency phenomena, while the quality of airborne and/or terrestrial data can be associated to medium and/or high(er) scale frequency bands. So, the whole spectrum of spaceborne/airborne/ground data systems covers all verifiable wave packages. Actually, the advantage of satellite lower frequency band data at the ground is their availability everywhere, while (airborne) medium and (terrestrial) high(er) frequency bands usually are at the disposal for regional and local occurrence, respectively. In this respect, a helpful tool for determining the depth and size is the introduction of known artificial disturbances such as monopoles in gravitation which superpose the original wave bands of the data in an easily predictable and calculable way.

Summarizing our results, we are led to the following conclusion: The multiscale approach which is presented in this contribution breaks up a complicated signal (like the gravitational field, the geomagnetic field) into "wave band signatures" at different scales, i.e., a certain resolution. To each scale parameter, a scaling function is defined leading to an approximation of the data at that certain resolution. The difference between two successive scaling functions, i.e., the wavelets, represents the corresponding wave bands and, thus, yields the desired geological detail information. With increasing scale, the approximation is getting finer and finer starting form a low pass approximation and adding more and more wave bands. The multiscale approach guarantees that the information contained on a certain

(coarse) level is also contained in the approximations of higher scales. It is advantageous that we are able to analyze the wave bands separately (decorrelation). Thus, this multiscale concept helps to find adaptive methods to the particular structure of the data. Additionally, the resolution of the model can be adapted to the spatial structures, i.e., for areas with coarse spatial structures, the resolution of the model can be chosen to be rather low and for areas with complicated structures the resolution can be increased accordingly. Consequently, since most data show correlation both in space as in frequency, the multiscale technique is an appropriate method for a simultaneous space and frequency localization. As far as the numerical realization is concerned, fast wavelet methods (FWT) are applicable.

Considering especially the disturbing potential field approximation in gravitation, we observe – from computational point of view – two main requirements: First, the field characteristics of geological features are usually of local character such that the use of local wavelets is evident. Second, in view of physical relevance of the multiscale approach, we need wavelets which have a certain relation to the corresponding partial differential equation (here: Laplace equation). Moreover, we have to be concerned with wavelet types which are manageable from mathematical point of view and, additionally, show a close relation to the physical model. Indeed, the developed multiscale method by means of regularizing wavelets using physically motivated fundamental solutions has its origins in works of the Geomathematics Group of the University of Kaiserslautern (see, e.g., [12, 15, 18, 20–22] and the list of references therein). The main results and characteristics of our studies presented here can be summarized as follows:

- Physically based behavior and appropriate interpretability of the developed wavelets.
- Numerical efficiency and economy of the wavelets by adaptive choice of the local support and resulting fast algorithms.
- Scale dependent correlation of wavebands and geological structures in a systematic "zooming-in / zooming out" decorrelation process.
- Specific transparency of certain geological structures for an appropriate choice of parameters.
- Depth determination and localization of geological formations by artificial point source disturbances.

Furthermore seen from the point of mathematical methodology, our multiscale (postprocessing) approach is not only restricted to potential methods involving the Laplace operator. Similar approaches can be formulated, e.g., for the Helmholtz and d'Alembert operators (cf. [2]).

Regarding the signature decorrelation and Haar-Type inversion, we deal with a construction of physically relevant wavelets based on the regularization of the fundamental solution for the decomposition of gravimetric data, and analyze different examples occurring in exploration. The decomposition of the 3D Marmousi density model shows a breakdown of the signals into their constituent components. Our numerical tests have further shown that the inversion technique described for

the local improvement of records is numerically stable. In particular, the method can be restricted to the specified local region of interest without changing the remaining area due to the local support of the wavelets. The resulting linear equation systems are sparse, hence, they can thus be solved efficiently and economically.

The particular advantage of the decorrelation method proposed here is the simultaneous calculation of the potential and the contrast function (density function) without any requirement of additional mathematical and numerical effort and this while closely ensuring physical relevance and numerically acceptable effort. It is therefore expected that the method presented here, in fact, will contribute substantially to minimizing the exploration risk, for example, in geothermal obligations by providing deeper and more secure geological information.

Acknowledgment

The authors thank the "Federal Ministry for Economic Affairs and Energy, Berlin" and the "Project Management Jülich" for funding the projects "GEOFÜND" (funding reference number: 0325512A, PI Prof. Dr. W. Freeden, University of Kaiserslautern, Germany) and "SPE" (funding reference number: 0324061, PI Prof. Dr. W. Freeden, CBM – Gesellschaft für Consulting, Business und Management mbH, Bexbach, Germany, corporate manager Prof. Dr. mult. M. Bauer).

References

[1] Bauer, M., Freeden, W., Jacobi, H., and Neu, T., Eds. (2014). *Handbuch Tiefe Geothermie*. Springer, Berlin, Heidelberg.

[2] Blick, C. (2015). *Multiscale Potential Methods in Geothermal Research: Decorrelation Reflected Post-Processing and Locally Based Inversion*. Ph.D.-thesis, Geomathematics Group, University of Kaiserslautern.

[3] Blick, C., Freeden, W., and Nutz, H. (2016). Feature Extraction of Geological Signatures by Multiscale Gravimetry. *GEM Int. J. Geomath.*, 8:57–83, 2017.

[4] Bruns, E.H. (1878). *Die Figur der Erde*. Königl. Preussisch. Geodätisches Institut, P. Stankiewicz Buchdruckerei, Berlin.

[5] Ernstson, K. (2018). Geologische und geophysikalische Untersuchungen. In Bauer, M., Freeden, W., Jacobi, H., and Neu, T., Eds., *Handbuch Oberflächennahe Geothermie*. Springer, Heidelberg.

[6] ESA (1996). The Nine Candidate Earth Explorer Missions. *Publications Division ESTEC, Noordwijk*, SP-1196(1).

[7] ESA (1998). European Views on Dedicated Gravity Field Missions: GRACE and GOCE. *An Earth Sciences Division Consultation Document*. ESD-MAG-REP-CON-001.

[8] ESA (1999). Gravity Field and Steady-State Ocean Circulation Mission. *Publications Division ESTEC, Noordwijk*, SP-1233(1). Report for mission selection of the four candidate earth explorer missions.

[9] Fehlinger, T. (2009). *Multiscale Formulations for the Disturbing Potential and the Deflections of the Vertical in Locally Reflected Physical Geodesy*. Ph.D.-thesis, Geomathematics Group, University of Kaiserslautern.

[10] Foulger, G., Natland, J., Presnall, D., and Anderson, D., Eds. (2005). *Plates, Plumes, and Paradigms*. Geological Society of America.

[11] Freeden, W. (1980). On Integral Formulas of the (Unit) Sphere and Their Application to Numerical Computation of Integrals. *Computing*, 25:131–146.

[12] Freeden, W. (1999). *Multiscale Modelling of Spaceborne Geodata*. B.G. Teubner, Leipzig.

[13] Freeden, W. and Blick, C. (2013). Signal Decorrelation by Means of Multiscale Methods. *World of Mining*, 65(5):304–317.

[14] Freeden, W., Fehlinger, T., Mayer, C., and Schreiner, M. (2008). On the Local Multiscale Determination of the Earth's Disturbing Potential from Discrete Deflections of the Vertical. *Comput. Geosc.*, 4:473–490.

[15] Freeden, W. and Gerhards, C. (2013). *Geomathematically Oriented Potential Theory*. CRC Press, Taylor & Francis, Boca Raton.

[16] Freeden, W., Gervens, T., and Schreiner, M. (1998). *Constructive Approximation on the Sphere* (*with Applications to Geomathematics*). Oxford Science Publications, Clarendon, Oxford.

[17] Freeden, W., Glockner, O., and Schreiner, M. (1998). Spherical Panel Clustering and Its Numerical Aspects. *J. Geodesy*, 72:586–599.

[18] Freeden, W. and Gutting, M. (2013). *Special Functions of Mathematical* (*Geo-*) *Physics. Applied and Numerical Harmonic Analysis* (*ANHA*). Birkhäuser, Basel.

[19] Freeden, W. and Hesse, K. (2002). On the Multiscale Solution of Satellite Problems by use of Locally Supported Kernel Functions Corresponding to Equidistributed Data on Spherical Orbits. *Stud. Sci. Math. Hung.*, 39:37–74.

[20] Freeden, W. and Michel, V. (2004). *Multiscale Potential Theory* (*with Applications to Geoscience*). Birkhäuser, Boston.

[21] Freeden, W. and Schreiner, M. (2006). Local Multiscale Modelling of Geoid Undulations From Deflections of the Vertical. *J. Geodesy*, 79:641–651.

[22] Freeden, W. and Schreiner, M. (2009). *Spherical Functions of Mathematical Geosciences* (*A Scalar, Vectorial, and Tensorial Setup*). Springer, Heidelberg.

[23] Freeden, W. and Wolf, K. (2008). Klassische Erdschwerefeldbestimmung aus der Sicht moderner Geomathematik. *Math. Semesterb.*, 56:53–77.

[24] Grafarend, E.W., Aardalan, A.A., and Finn, G. (2006). Ellipsoidal Vertical Deflections and Ellipsoidal Gravity Disturbances: Case Studies. *Stud. Geophys. Geod.*, 50:1–57.

[25] Grafarend, E.W., Klapp, M., and Martinec, Z. (2015). Spacetime Modeling of the Earth's Gravity Field by Ellipsoidal Harmonics. In Freeden, W., Nashed, M.Z., and Sonar, T., Eds., *Handbook of Geomathematics*, volume 1, 381–496. Springer, New York, 2nd edition.

[26] Grant, E.S. and West, G.F. (1965). *Interpolation Theory in Applied Geophysics*. McGraw-Hill Book Company.

[27] Groten, E. (1979). *Geodesy and the Earth's Gravity Field I + II*. Dümmler, Bonn.

[28] Gutting, M. (2008). *Fast Multipole Methods for Oblique Derivative Problems*. Ph.D.-thesis, Geomathematics Group, University of Kaiserslautern.

[29] Gutting, M. (2012). Fast Multipole Accelerated Solution of the Oblique Derivative Boundary-Value Problem. *GEM Int. J. Geomath.*, 2:223–252.

[30] Gutting, M. (2015). Fast Spherical/Harmonic Spline Modeling. In Freeden, W., Nashed, M.Z., and Sonar, T., Eds., *Handbook of Geomathematics*, volume 3,2711–2746. Springer, New York, 2nd. edition.

[31] Harpp, K.S., Fornari, D.J., Geist, D.J., and Kurz, M.D. (2003). A Manifestation of Plume-Ridge Interaction in the Northern Galapagos Islands. *Geochemistry, Geophysics, Geosystems*, 4(9):DOI: 10.1029/2003GC000531.

[32] Heiskanen, W.A. and Moritz, H. (1967). *Physical Geodesy*. Freeman, San Francisco.

[33] Helmert, F. (1884). *Die Mathematischen und Physikalischen Theorien der Höheren Geodäsie, I, II*. B.G. Teubner, Leipzig.

[34] Hesse, K. (2003). *Domain Decomposition Methods in Multiscale Geopotential Determination from SST and SGG*. Ph.D.-thesis, Geomathematics Group, University of Kaiserslautern.

[35] Hesse, K., Sloan, I.H., and Womersley, R.S. (2015). Numerical Integration on the Sphere. In Freeden, W., Nashed, M.Z., and Sonar, T., Eds., *Handbook of Geomathematics*, volume 2, 2671–2710. Springer, New York, 2nd edition.

[36] Hofmann-Wellenhof, B. and Moritz, H. (2005). *Physical Geodesy*. Springer, Wien, New York.

[37] IEA (2012). Iceland Country Report 2012. Report, IEA Geothermal.

[38] Jacobs, F. and Meyer, H. (1992). *Geophysik-Signale aus der Erde*. B.G. Teubner, Leipzig, and VDF Verlag, Zürich.

[39] Keating, P. (1992). Interpretation of the Gravity Anomaly Field in the Noranda Val d'Or region, Abitibi Greenstone Belt, Canadian Shield. *Can. J. Earth Sciences*, 29(5):962–971.

[40] Kellogg, O.D. (1967). *Foundations of Potential Theory*. Springer Berlin, Heidelberg, New York.

[41] Kusche, J. (2015). Time-Variable Gravity Field and Global Deformation of the Earth. In Freeden, W., Nashed, M.Z., and Sonar, T., Eds., *Handbook of Geomathematics*, volume 1, 321–338. Springer, New York, 2nd edition.

[42] Martin, G.S., Wiley, R., and Marfurt, K.J. (2006). Marmousi2: An Elastic Upgrade for Marmousi. *The Leading Edge*, 25(2):156–166.

[43] Mathar, D. (2008). *Wavelet Variances and Their Application in Geoscientifically Relevant Feature Detection*. Diploma thesis, University of Kaiserslautern, Geomathematics Group.

[44] Meinesz, F.A.V. (1928). A Formula Expressing the Deflection of the Plumb Line in the Gravity Anomalies and Some Formulas for the Gravity Field and the Gravity Potential Outside the Geoid. *Proc. Koninklijke Akad. Wet. Amsterdam*, 31:315–322.

[45] Meissl, P.A. (1971). A Study of Covariance Functions Related to the Earth's Disturbing Potential. Scientific Report No. 151, The Ohio State University, Department of Geodetic Science, Columbus.

[46] Michel, V. (2002). *A Multiscale Approximation for Operator Equations in Separable Hilbert Spaces – Case Study: Reconstruction and Description of the Earth's Interior*. Habilitation thesis, Geomathematics Group, University of Kaiserslautern. Shaker, Aachen.

[47] Michel, V. and Fokas, A.S. (2008). A Unified Approach to Various Techniques for the Non-Uniqueness of the Inverse Gravimetric Problem and Wavelet-Based Methods. *Inverse Problems*, 24 045019 (25 pp.), DOI: 10.1088/0266-5611/24/4/045019.

[48] Militzer, H. and Weber, F. (1984). *Angewandte Geophysik, Band* 1*, Gravimetrie und Magnetik*. Springer, Wien, New York.

[49] Möhringer, S. (2014). *Decorrelation of Gravimetric Data*. Ph.D.-thesis, Geomathematics Group, University of Kaiserslautern.

[50] Morgan, W.J. (1971). Convection Plumes in the Lower Mantle. *Nature*, 230:42–43.

[51] Moritz, H. (2015). Classical Physical Geodesy. In Freeden, W., Nashed, M.Z., and Sonar, T., Eds., *Handbook of Geomathematics*, volume 1, 253–289. Springer, New York, 2nd. edition.

[52] Nations, U. (2010). Current and Planned Global and Regional Navigation Satellite Systems and Satellite-Based Augmentations Systems. In *Proceedings of ICG*.

[53] Nettleton, L.L. (1971). *Elementary Gravity and Magnetics for Geologists and Seismologists*. Society Of Exploration Geophysicists, Tulsa, OK.

[54] Nettleton, L.L. (1976). *Gravity and Magnetics in Oil Prospecting*. McGraw-Hill, New York.

[55] Neumann, F. (1887). *Vorlesungen über die Theorie des Potentials und der Kugelfunktionen*. B.G. Teubner, Leipzig.

[56] Pizzetti, P. (1894). Geodesia – sulla espressione della gravità alla superficie del geoide, supposto ellissoidico. *Att. R. Acad. Lincei*, 3:331–350.

[57] Pizzetti, P. (1909). Corpi equivalenti rispetto alla attrazione newtoniana esterna. *Rom. Acc. L. Rend.*, 18:211–215.

[58] Ritter, J. and Christensen, U. (2007). *Mantle Plumes, A Multidisciplinary Approach*. Springer, Berlin, Heidelberg.

[59] Rivas, J. (2009). Gravity and Magnetic Methods. In *Short Course on Surface Exploration for Geothermal Resources*.

[60] Rummel, R. (1997). Spherical Spectral Properties of the Earth's Gravitational Potential and Its First and Second Derivatives. In Sansò, S. and Rummel, R., Eds., *Geodetic Boundary Value Problems in View of the One Centimeter Geoid*, volume 65 of *Lecture Notes in Earth Science*, 359–404. Springer, Berlin, Heidelberg.

[61] Rummel, R. (2015). GOCE: Gravitational Gradiometry in a Satellite. In Freeden, W., Nashed, M.Z., Eds., *Handbook of Geomathematics*, volume 1, 211–226. Springer, New York, 2nd edition.

[62] Rummel, R., Balmino, G., Johannessen, J., Visser, P., and Woodworth, P. (2002). Dedicated Gravity Field Missions – Principles and Aims. *J. Geodyn.*, 33:3–20.

[63] Schuber, D., Turcotte, D., and Olson, P. (2001). *Mantle Convection in the Earth and Planets*. Cambridge University Press, Cambridge.

[64] Seigel, H.O. (1995). *A Guide to High Precision Land Gravimeter Surveys*. Scintrex Limited, Concord, Ontario.

[65] Stokes, G.G. (1849). On the Variation of Gravity at the Surface of the Earth. *Trans. Cambr. Phil. Soc.*, 148:672–712.

[66] Stokes, G.G. (1867). On the internal distribution of matter which shall produce a given potential at the surface of a gravitating mass. *Proc.Royal Soc. London*, 15:482–486.

[67] Symes, W.W. (2014). T.R.I.P. the Rice inversion project, Department of Computational and Applied Mathematics, Rice University, Houston, Texas, USA. URL: http://www.trip.caam.rice.edu/downloads/downloads.html, accessed 12. September 2016.

[68] Torge, W. (1989). *Gravimetry*. de Gruyter, Berlin.

[69] Torge, W. (1991). *Geodesy*. de Gruyter, Berlin.

[70] Tykhonov, A.N. (1963). Solution of Incorrectly Formulated Problems and the Regularization Method. *Sov. Math.*, 5:1035–1038. (translation from *Dokl. Akad. Nauk*, (15):501–504).

[71] Wikipedia (2016). Galápagos hotspot. URL: https://en.wikipedia.org/wiki/Galapagos_hotspot, accessed 12. May 2016.

[72] Wilson, J. (1963). A Possible Origin of the Hawaiian Island. *Can. J. Phys.*, 41:863–868.

[73] Wolf, K. (2009). *Multiscale Modeling of Classical Boundary Value Problems in Physical Geodesy by Locally Supported Wavelets*. Ph.D.-thesis, Geomathematics Group, University of Kaiserslautern.

C. Blick, W. Freeden, and H. Nutz
Geomathematics Group
University of Kaiserslautern
MPI-Gebäude, Paul-Ehrlich-Str. 26
D-67663 Kaiserslautern, Germany